Title

The Role of Spin—Orbit Coupling in the Linear Absorption Spectrum and Intersystem Crossing Rate Coefficients of Ruthenium Polypyridyl Dyes

Journal

The Journal of Physical Chemistry A, 128(37)

ISSN

1089-5639

Authors

Talbot, Justin J

Cheshire, Thomas P

Cotton, Stephen J

et al.

Publication Date

2024-09-19

DOI

10.1021/acs.jpca.4c04122

The Role of Spin-Orbit Coupling in the Linear Absorption Spectrum and Intersystem Crossing Rate Coefficients of Ruthenium Polypyridyl Dyes

Justin J. Talbot,[†] Thomas P. Cheshire,[‡] Stephen J. Cotton,[†] Frances A. Houle,[‡] and Martin Head-Gordon[*,†]

[†]*Department of Chemistry, University of California, Berkeley, California 94720, USA*

[‡]*Chemical Sciences Division, Lawrence Berkeley National Laboratory, Berkeley, California, 94720*

E-mail: mhg@cchem.berkeley.edu

Abstract

The successful use of molecular dyes for solar energy conversion requires efficient charge injection, which in turn requires the formation of states with sufficiently long lifetimes (e.g. triplets). The molecular structure elements that confer this property can be found empirically, however computational predictions using *ab initio* electronic structure methods are invaluable to identify structure-property relations for dye sensitizers. The primary challenge for simulations to elucidate the electronic and nuclear origins of these properties is a spin-orbit interaction which drives transitions between electronic states. In this work, we present a computational analysis of the spin-orbit corrected linear absorption cross sections and intersystem crossing rate coefficients for a derivative set of phosphonated tris(2,2'-bipyridine)ruthenium(2+) dye molecules. After sampling the ground state vibrational distributions, the predicted linear absorption

cross sections indicate that the mixture between singlet and triplet states plays a crucial role in defining the line shape of the metal-to-ligand charge transfer bands in these derivatives. Additionally, an analysis of the intersystem crossing rate coefficients suggests that transitions from the singlet into the triplet manifolds are ultrafast with rate coefficients on the order of 10^{13} s^{-1} for each dye molecule.

Introduction

Dye sensitization of photovoltaic systems, such as traditional light harvesting[1–3] and photoelectrosynthesis cells,[4–8] offers the potential for the low-cost generation of solar energy. These systems are constructed by coating a metal-oxide surface, such as TiO_2, with a molecular dye designed to absorb visible radiation and inject the excited electrons into a high band gap semiconductor.[9–11] Although significant design improvements are required to use these systems at scale,[12,13] current reports of power conversion efficiencies for dye-sensitized solar cells are between 10%–15% under direct sunlight and over 25% under ambient lighting.[14–17] Employing dye molecules to promote the injection of electrons is beneficial since the ligand framework can be specially designed to tune various structure-property relationships resulting in greater power conversion efficiencies.[18–20]

Extensive experimental[21–25] and theoretical[26–30] studies have been dedicated to the optimization and discovery of dye molecules. Of the many dye molecules proposed, ruthenium polypyridyl complexes have emerged as promising candidates due to to their distinctive metal-to-ligand charge transfer (MLCT) bands which are found in the $400 - 500$ nm region of the absorbance spectrum. The most studied molecule in this class is tris(2,2'-bipyridine)ruthenium(2+) (RuBPY) where experiments and simulations probing the MLCT band have been instrumental in understanding photoinduced phenomena such as intersystem and internal conversion,[31–34] electron and charge transfer dynamics,[35–38] and the influence of molecular vibrations and solvent/surface environment on excited electronic states.[39–43] RuBPY is typically tethered to a metal-oxide surface using functional groups and,

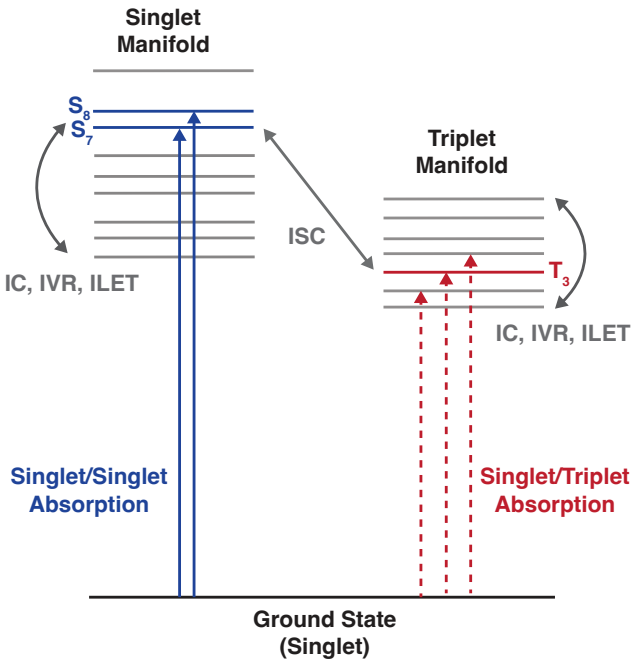

Figure 1: A diagram illustrating some radiative and non-radiative transitions in RuBPY. The radiative transitions include singlet-to-singlet and direct singlet-to-triplet absorption. The nonradiative transitions include internal conversion (IC), intramolecular vibrational energy redistribution (IVR), interligand electron transfer (ILET), and spin-orbit mediated intersystem crossing (ISC) between singlet and triplet states. Some of the primary states involved in the linear absorption and ISC (S_7, S_8 (blue) and T_3 (red)) are highlighted.

while many groups have been proposed, phosphonated derivatives are particularly robust—exhibiting considerably greater stability and higher conversion efficiencies in comparison to their alternatively-functionalized counterparts.[44–48]

One approach that improves the performance of dye molecules as photosensitizers is to employ functional groups to tune the transitions between excited electronic states.[49–54] An illustration highlighting some competing transitions in RuBPY is shown in Fig. 1. After an electron is excited from the ground singlet state into the singlet manifold, a series of nonradiative relaxations, such as internal conversion,[55,56] intramolecular vibrational energy redistribution,[57,58] and/or interligand electron transfer[59,60] can drive transitions between the singlet electronic states. Additionally, the electron may undergo intersystem crossing into the triplet manifold where similar nonradiative pathways are possible.

Although the transitions between singlet and triplet states depends on the slow nuclear

motion of the ligands, intersystem crossing is generally considered to be highly efficient in derivatives of RuBPY with ϕ_{ISC} reported between 0.5 and 1 in our recent analysis of spectroscopic data for solution phase dyes using kinetics methods.[61,62] The intersystem crossing is also ultrafast as confirmed by femtosecond fluorescence experiments where it is predicted to be within 100 fs in solution.[63–65] Although considerably faster than reported for the condensed phase, recent *ab initio* simulations on gas phase RuBPY predict similar time scales with nearly 70% of the population in the excited singlet manifold undergoing intersystem crossing within 30 fs.[55]

Employing *ab initio* quantum chemistry methods that include spin-orbit coupling (SOC) can aid in elucidating the electronic and nuclear rearrangements that drive intersystem crossing.[66] Some of the more sophisticated and accurate variational approaches at the Hartree-Fock and density functional level include spin-orbit coupling *a priori* when optimizing the self-consistent field equations. Such methods include the two-component (X2C),[67–71] Douglas-Kroll-Hess (DKH),[72,73] and the zeroth-order regularization approximation (ZORA).[74,75] For larger system sizes directly amenable to time-dependent density functional theory (TDDFT) however, these variational approaches can become cost prohibitive.[76] In such cases, simpler approaches become appropriate where the Tamm-Dancoff approximation (TDA) provides a wavefunction-like approximation to spin pure states (i.e. those with integer total angular momentum L and total spin S) which are then mixed together using perturbation theory.[77] Alternatively, including spin-orbit coupling in designer excited state wavefunctions of the multiconfigurational or complete active space type have been proposed which incorporate both perturbative and variational approaches.[78–81]

In this work, TDDFT/TDA and perturbation theory were employed to analyze the intersystem crossing rate coefficients and assign the electronic transitions of the MLCT bands for RuBPY and a set of phosphonated derivatives (labeled RuP, RuP2, and RuP3). The objective of this work is to permit an in-depth understanding of the nuclear and electronic rearrangements that underlie our prior kinetics analysis of the spectroscopic signatures of

these dyes.[53,61,62] The article is organized as follows: first, we outline a protocol for applying a SOC correction to TDDFT/TDA states. Then, the SOC states are used to calculate corrected linear absorption cross sections and intersystem crossing rate coefficients. The analysis presented here highlights the distinct role that singlet-to-triplet transitions have on the kinetics and linear absorption probabilities in these molecular dyes and validate several rate coefficients for the intersystem crossing steps that were reported in our previous study.

Methods

The following notation is used throughout this work: a spin-pure electronic state I with integer spin S and spin projection M is denoted as $|\Psi_I^{S,M}\rangle$. Occupied molecular orbitals are denoted with indexes i and j and virtual orbitals are denoted using a and b. Lower-case subscripts μ and ν denote integrals over atomic orbital (AO) basis functions. In this work, only spin pure singlet and triplet states generated from a restricted Kohn-Sham determinant are considered.

Perturbative Spin-Orbit Coupling

The Breit-Pauli (BP) SOC Hamiltonian is a perturbative, two-electron relativistic correction to the adiabatic electronic Hamiltonian. The benefit of using the BP Hamiltonian is that the spin-orbit (SO) and spin-other-orbit (SOO) interactions from this two-electron Hamiltonian are contracted into single terms.[82,83] The BP Hamiltonian has the form:

$$\hat{H}_{BP} = \sum_i \hat{h}^{SO}(i) \cdot \hat{s}(i) + \sum_{i \neq j} \hat{h}^{SOO}(i,j) \cdot \Big(\hat{s}(i) + 2\hat{s}(j) \Big), \tag{1}$$

where the one-electron SO operator is

$$\hat{h}^{SO}(i) \equiv \frac{\alpha_0^2}{2} \sum_A \frac{Z(A)}{\hat{r}_{iA}^3} (\vec{\hat{r}}_{iA} \times \vec{\hat{p}}_i),$$

and the two-electron SOO operator is

$$\hat{h}^{SOO} \equiv \frac{\alpha_0^2}{2} \frac{1}{\hat{r}_{ij}^3} (\vec{r}_{ij} \times \vec{\hat{p}}_i),$$

where α_0 is the fine structure constant, $\hat{r}_{iA}$ is the distance between electron i and nucleus A, $\hat{r}_{ij}$ is the distance between electrons i and j, $\hat{s}_i$ is the spin and $\hat{p}_i$ is the momentum operator of electron i, and Z_A is the nuclear charge.

Matrix elements of the BP Hamiltonian are computed by contracting the integrals of $\hat{h}$ with one- and two-particle density matrices (labeled 1PDM and 2PDM respectively). However, evaluating and contracting the two-electron SOO integrals is known to be a computational bottleneck.[84,85] To alleviate this cost, the SOO interactions are commonly approximated using effective 1-electron SOC operators of the mean-field type.[86] An alternative approach, and the one used for this work, is to include the SOO interactions empirically in the 1-electron SO operator through the use of an effective nuclear charge:

$$\tilde{H}_{BP} = \sum_i \tilde{h}(i) \cdot \hat{s}(i) \tag{2}$$

where the effective 1-electron orbital angular momentum operator

$$\tilde{h}(i) \equiv \frac{\alpha_0^2}{2} \sum_A \frac{Z_{\text{eff}}(A)}{\hat{r}_{i,A}^3} \left(\vec{\hat{r}}_{i,A} \times \vec{\hat{p}}_i \right) \tag{3}$$

has the same form as in Eq. 1 except that the nuclear charge $Z(A)$ has been replaced with an empirical parameter $Z_{\text{eff}}(A)$. Tabulated values for this parameter are available in the literature where they have been fit to reproduce experimentally measured fine structure splittings for each atom.[87] The values used for $Z_{\text{eff}}(A)$ in this work are provided in Table S2 of the supporting information.

Using first-order perturbation theory, matrix elements of the BP Hamiltonian in Eq. 2 can be calculated using the Wigner-Eckart theorem:

$$\langle \Psi_I^{S',M'} | \, \tilde{H}_{BP} \, | \Psi_J^{S'',M''} \rangle = \sum_m^{0,\pm 1} (-1)^m \begin{pmatrix} S'' & 1 & S' \\ M'' & m & M' \end{pmatrix} \mathbf{P}^{I,J}_{S',S''} \cdot \tilde{h}^{(m)}, \tag{4}$$

which involves evaluating a Clebsch-Gordan (CG) coefficient (expressed here as a 3-j symbol) and contracting a 1PDM ($\mathbf{P}^{I,J}_{S',S''}$) with the 1-electron orbital angular momentum integrals ($\tilde{h}^m$). [1] The 1-electron orbital angular momentum integrals:

$$\tilde{h}^{(0)}_{\mu\nu} = \tilde{h}^{(z)}_{\mu\nu} \tag{5a}$$

$$\tilde{h}^{(+1)}_{\mu\nu} = \frac{1}{\sqrt{2}} \left(\tilde{h}^{(x)}_{\mu\nu} + i \tilde{h}^{(y)}_{\mu\nu} \right) \tag{5b}$$

$$\tilde{h}^{(-1)}_{\mu\nu} = \frac{1}{\sqrt{2}} \left(\tilde{h}^{(x)}_{\mu\nu} - i \tilde{h}^{(y)}_{\mu\nu} \right), \tag{5c}$$

are those from Eq. 3 which are evaluated over Cartesian AO basis functions and then expressed in the spherical tensor basis.

In the TDA, excitations are decoupled from de-excitations which enables a wavefunction-like expression for the excited states.[89] The singlet excited states have the following form:

$$|\Psi_I^{0,0}\rangle = \frac{1}{\sqrt{2}} \sum_{ai} s^I_{ai} \left(\, |\Phi^{\bar{a}}_{\bar{i}}\rangle + |\Phi^a_i\rangle \, \right) \tag{6}$$

where s^I_{ai} is the amplitude and $|\Phi^{\bar{a}}_{\bar{i}}\rangle$ denotes a singly-excited determinant which is created after promoting an electron from a β occupied spin orbital i to a β virtual orbital a. Likewise, $|\Phi^a_i\rangle$ (i.e. with no bar above i or a) denotes the promotion of an α electron. The triplet excited states have the form:

[1] Actually, the 1PDM is scaled by an inverse CG coefficient as a result of evaluating a reduced matrix element.[88]

$$|\Psi_J^{1,0}\rangle = \frac{1}{\sqrt{2}} \sum_{ai} t_{ai}^J \Big(|\Phi_{\bar{i}}^{\bar{a}}\rangle - |\Phi_i^a\rangle \Big) \tag{7a}$$

$$|\Psi_J^{1,1}\rangle = \sum_{ai} t_{ai}^J |\Phi_i^{\bar{a}}\rangle \tag{7b}$$

$$|\Psi_J^{1,-1}\rangle = \sum_{ai} t_{ai}^J |\Phi_{\bar{i}}^{a}\rangle \,, \tag{7c}$$

where t_{ai}^J denotes the triplet amplitudes which are independent of spin projection m.

After expressing the singlet and triplet amplitudes from Eq. 6 and Eq. 7 as rectangular matrices ($\mathbf{t}_{\mathrm{vo}}^J$ and $\mathbf{s}_{\mathrm{vo}}^I$), the scaled 1PDM between the Kohn-Sham reference and an excited triplet state is:

$$\mathbf{P}_{1,0}^{J,0} = \mathbf{C}_v \mathbf{t}_{vo}^J \mathbf{C}_o^\dagger, \tag{8}$$

the singlet-to-triplet scaled 1PDM is:

$$\mathbf{P}_{1,0}^{I,J} = \mathbf{C}_v \mathbf{t}_{vo}^I \mathbf{s}_{vo}^{J\dagger} \mathbf{C}_v^\dagger - \mathbf{C}_o \mathbf{s}_{vo}^{J\dagger} \mathbf{t}_{vo}^I \mathbf{C}_o^\dagger, \tag{9}$$

and the excited triplet-to-triplet scaled 1PDM is:

$$\mathbf{P}_{1,1}^{I,J} = \sqrt{2}\Big(\mathbf{C}_v \mathbf{t}_{vo}^I \mathbf{t}_{vo}^{J\dagger} \mathbf{C}_v^\dagger + \mathbf{C}_o \mathbf{t}_{vo}^{J\dagger} \mathbf{t}_{vo}^I \mathbf{C}_o^\dagger \Big), \tag{10}$$

where $\mathbf{C}_o$ and $\mathbf{C}_v$ are rectangular matrices which contain the occupied and virtual blocks of the molecular orbital coefficient matrix $\mathbf{C}$.

In order to solve for the SOC states, the BP Hamiltonian is built, added to the TDDFT/TDA Hamiltonian H_0 which is expressed in the basis defined in Eq. 6 and Eq. 7, and diagonalized.[90,91] The resulting SOC eigenstates contain contributions from the ground state $|\Psi_0^{0,0}\rangle$, a chosen number a excited singlet states $|\Psi_I^{0,0}\rangle$, and a chosen number of three-fold degenerate

excited triplet states $|\Psi_J^{1,m}\rangle$ with spin $m = 0, \pm 1$. The SOC excited state wavefunction is:

$$|\Psi_N\rangle = C_0' \, |\Psi_0^{0,0}\rangle + \sum_I^{N_S} C_I \, |\Psi_I^{0,0}\rangle + \sum_m^{0,\pm 1} \sum_J^{N_T} C_{J,m} \, |\Psi_J^{1,m}\rangle \,, \tag{11}$$

where N_S and N_T denote the number of singlet and triplet states included in the perturbation and C_I and $C_{J,m}$ are the amplitudes for the singlet and triplet contributions respectively. When basis states from a restricted Kohn-Sham determinant are employed, the ground state is:

$$|\Psi_0\rangle = C_0 \, |\Psi_0^{0,0}\rangle + \sum_m^{0,\pm 1} \sum_J^{N_T} C_{J,m}' \, |\Psi_J^{1,m}\rangle \,, \tag{12}$$

since the scaled 1PDM of Eq. 8 can only couple together excited states in the triplet manifold to the singlet ground state,

Transition Dipole Integrals

Applying the BP correction to the linear absorption spectrum requires the transition dipole moment integrals between the SOC states. Since the dipole operator is independent of both spin and spin projection, the SOC corrected transition dipole integrals are:

$$\langle \Psi_N | \, \hat{\mu} \, | \Psi_0 \rangle = \hat{\mu}_{0,0} + \hat{\mu}_{S,0} + \hat{\mu}_{T,T}, \tag{13}$$

where the subscripts denote ground (0), singlet (S), and triplet (T) contributions. The ground-to-ground state contribution is

$$\hat{\mu}_{0,0} \equiv C_0'^{*} \, \langle \Psi_0^{0,0} | \, \hat{\mu} \, | \Psi_0^{0,0} \rangle \, C_0,$$

the ground-to-singlet excited state contribution is

$$\hat{\mu}_{S,0} \equiv \sum_I C_I^{*} \, \langle \Psi_I^{0,0} | \, \hat{\mu} \, | \Psi_0^{0,0} \rangle \, C_0,$$

and a triplet-to-triplet excited state contribution is

$$\hat{\mu}_{T,T} \equiv \sum_{m}^{0,\pm1} \sum_{J'J} C'^{*}_{J',m} \langle \Psi^{1,m}_{J'} | \, \hat{\mu} \, | \Psi^{1,m}_{J} \rangle \, C_{J,m},$$

which are simply the spin-pure transition dipole moment integrals weighted by the complex amplitudes C_0, C_I and $C_{J,m}$.

Nuclear Ensemble Method

The linear absorption spectra were predicted using the nuclear ensemble method—which is a simulation-based approach that samples the transition dipole integrals and excitation energies from a ground vibrational state distribution.[92,93] The main idea of this approach is that the linear absorption cross section can be sampled stochastically:[94]

$$\sigma(E) = \frac{\pi E}{3\hbar\epsilon_0 c} \sum_{b} \int \rho_0\big(\vec{R}\big) \left| \mu_{b0}\big(\vec{R}\big) \right|^2 g(\Delta, \delta) d\vec{R} \tag{14}$$

with

$$\Delta \equiv E - E_{b0}\big(\vec{R}\big),$$

where $\rho_0\big(\vec{R}\big)$ is the ground state vibrational distribution and $E_{b0}(\vec{R})$ are the ground-to-excited state transition energies. The broadening function:

$$g(\Delta, \delta) = \sqrt{\frac{2}{\pi}} \frac{\hbar}{\delta} \exp\left(- \frac{2\Delta^2}{\delta^2} \right) \tag{15}$$

used here was chosen to be a Gaussian which contains an empirical parameter δ.

Intersystem Crossing Rate Coefficients

The intersystem crossing rate coefficients (k_{ISC}) were calculated using Marcus theory:[95,96]

$$k_{\mathrm{ISC}}^{IJ} = \frac{1}{\hbar}\left(V_{\mathrm{SOC}}^{IJ}\right)^2 \sqrt{\frac{\pi}{\lambda k_B T}} \exp\left(-\frac{(\lambda + \Delta G_0)^2}{4\lambda k_B T}\right) \tag{16}$$

where λ denotes the reorganization energy, ΔG_0 is the driving force, and

$$V_{\mathrm{SOC}}^{IJ} = \sqrt{\sum_{m}^{0,\pm 1} |\left\langle \Psi_I^{0,0} \right| \tilde{H}_{\mathrm{BP}} \left| \Psi_J^{1,m} \right\rangle|^2} \tag{17}$$

is the spin-orbit coupling constant.[97] The harmonic, parallel, and vertical gradient approximations were employed for the reorganization energies and driving forces.[98] Under these approximations, the reorganization energy is defined as the sum of the individual normal mode contributions:

$$\lambda = \sum_j \frac{1}{2\mu_j \omega_j^2} \left(\frac{\partial E_J}{\partial Q_j}\right)_{S_{I,min}}^2 \tag{18}$$

where μ_j and ω_j denote the reduced mass and harmonic frequency of normal mode j, $\frac{\partial E_J}{\partial Q_j}$ is the TDDFT/TDA energy gradient of the final triplet state J, and $S_{I,min}$ denotes that the gradient is evaluated at the minimum energy configuration of the initial singlet state.

Computational Details

The excitation energies, SOC integrals, excited state amplitudes, and transition dipole integrals were calculated using a development version of the Q-Chem 6.1 software package.[99] An investigation into the basis set and functional dependence of the MLCT transitions for RuBPY was performed and the B3LYP/def2-SVP-PP level of theory was chosen for all calculations since it had the lowest absolute error when compared with experiment. Further details and electronic structure benchmarks are provided in Fig. S1 of the supporting information.

Geometry optimizations were performed on the ground singlet state for each dye molecule. At the optimized geometries, the BP Hamiltonian from Eq. 4 was expressed in a basis

including the ground state, the lowest ten singlet states, and the lowest 30 triplet states (i.e. the lowest ten three-fold degenerate triplet states) and diagonalized. As justified in Table S1 of the supporting information, higher-lying states (i.e. those above the MLCT bands) were found to be insignificant. In all dye molecules, SOC corrections to the ground state were found to be negligible (i.e. $|C_0|^2 = 1$) which allowed the singlet and triplet percent contribution of each *excitation* to be decomposed according to that of the final state:

$$P_S = \sum_{I}^{N_S} |C_I|^2 \tag{19a}$$

$$P_T = \sum_{m}^{0,\pm1} \sum_{J}^{N_T} |C_{J,m}|^2, \tag{19b}$$

where the coefficients C_I and $C_{J,m}$ are from Eq. 11. Likewise, the negligible SOC corrections to the ground state allowed the orbital excitation character to be decomposed according to the amplitudes of the final state:

$$\left|X_{ai}\right|^2 = \sum_{I}^{N_S} \left|C_I s_{ai}^I\right|^2 + \sum_{m}^{0,\pm1} \sum_{J}^{N_T} \left|C_{J,m} t_{ai}^J\right|^2 \tag{20}$$

where X_{ai} denotes the complex valued transition amplitude between an occupied molecular orbital i and virtual orbital a.

The SOC excitation energies and oscillator strengths were used to calculate the linear absorption cross sections. At the optimized ground state geometry for each dye molecule, a harmonic frequency analysis was performed and the resulting normal modes were employed to sample ≈ 2000 configurations from a $T = 300K$ Wigner distribution. A Gaussian broadening function was chosen (see Eq. 15) with the broadening parameter $\delta = 0.1$ eV. Further analysis of this parameter is provided in Fig. S8 of the supporting information. For comparison, the experimental linear absorption cross sections for RuBPY were obtained from Ref. 100 and

the experimental linear absorption cross sections for RuP, RuP2, and RuP3 were obtained from Ref. 61 and Ref. 62.

The spin-pure TDDFT/TDA excitation energies and the SOC constants from Eq. 17 were used to calculate the intersystem crossing rate coefficients. For these calculations, the geometries of four excited singlet states S_5 - S_8 were optimized. The effects of internal conversion were included using a state following algorithm which optimizes the geometry of the excited state based on orbital excitation character.[101] Using state following allows the geometry optimization to "jump" electronic states based off of the character of the molecular orbitals. Therefore, the optimized excited-state geometries are those that best represent the orbital excitation character from the ground state configuration. The lower-lying electronic states S_1 - S_4 were not included due to their negligible oscillator strengths.

At the minimum on each excited state potential energy surface, frequency calculations were performed to obtain the excited state harmonic frequencies and reduced masses. All frequencies were found to be real and positive except for the S_8 excited state of RuBPY which had one imaginary frequency ($\omega = 185i$ cm^{-1}). This frequency and corresponding normal mode were removed from the calculation (see Fig. S7 of the supporting information). The reorganization energies were calculated according to Eq. 18 and the driving forces were calculated as a sum (or difference) of the excitation energies of the initial singlet state and the vertical excitation (or de-excitation) energies of the final triplet states (see Fig. S6). The calculation of the driving force and reorganization energy were performed in the gas phase and solvent effects were neglected. The mode-specific reorganization energies, spin-orbit coupling constants, and driving forces are provided in the supporting information (ISC.xlsx).

Results and Discussion

The B3LYP/def2-SVP-PP optimized geometries of RuBPY and the three phosphonated derivatives are shown in Fig. 2. Of the derivatives, RuBPY is the only one with point group

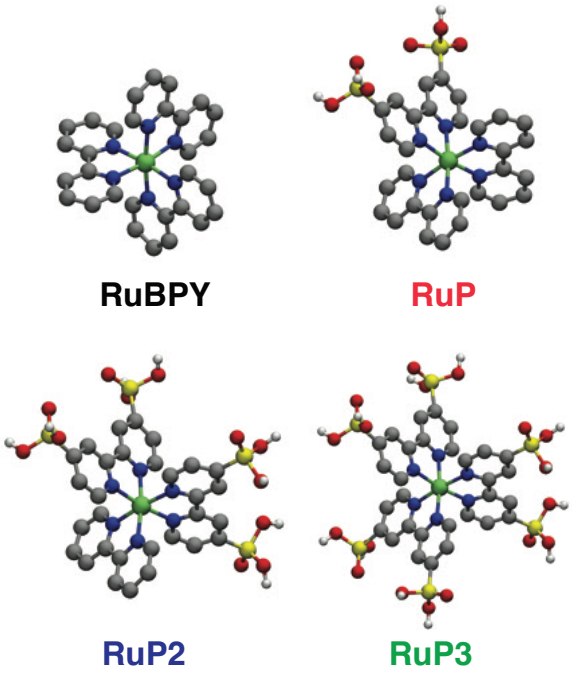

Figure 2: The B3LYP/def2-SVP-PP optimized geometries of the ruthenium polypyridyl dye molecules. The geometry of RuBPY (top left), RuP (top right), RuP2 (bottom left) and RuP3 (bottom right). The hydrogen atoms on the bipyridine ligands have been removed for clarity. The atom color coding is gray (C), blue (N), green (Ru), yellow (P), white (H), and red (O).

symmetry (D_3) where three bipyridine ligands are attached to a central ruthenium atom. The structures RuP, RuP2, and RuP3 have two phosphonic acid groups attached to one, two, and three of the bipyridine ligands, respectively. The optimized geometries correspond to minimum energy configurations—as confirmed by a harmonic frequency analysis—on the singlet ground state potential energy surfaces. The optimizations, and all subsequent calculations, were performed in the gas phase with a +2 charge. There were no counter ions present. Although there is a low-lying C_2 isomer for RuBPY,[102] the minimum energy configuration was confirmed to have D_3 point group symmetry.

The frontier molecular orbitals of RuBPY are shown in Fig 3. In the occupied space, the pyridine orbitals transform according to the a_1 and e irreducible representations. The highest occupied molecular orbital (HOMO) has a_1 symmetry, and although there is a pyridine orbital with a_1 symmetry that is allowed to mix, the HOMO has primarily ruthenium $4d_{z^2}$

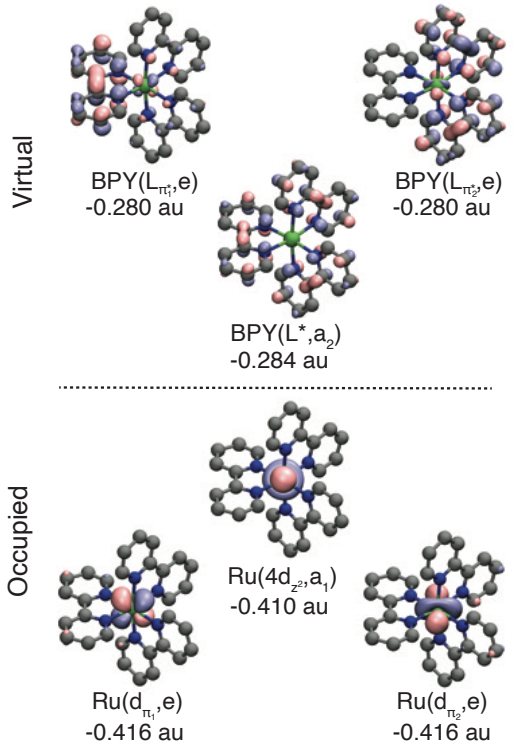

Figure 3: The frontier molecular orbitals of RuBPY. Orbital energies (in au) and symmetries (D_3) are displayed below each orbital. The occupied orbitals are a degenerate pair of π-type orbitals (labeled d_{π_1} and d_{π_2}) with e symmetry and the a_1 symmetry HOMO orbital which has primarily ruthenium $4d_{z^2}$ character. In the virtual space, the LUMO is a ligand-only orbital (labeled L^* with a_2 symmetry) followed by a degenerate pair of e symmetry π^*-type orbitals (labeled $L_{\pi_1^*}$ and $L_{\pi_2^*}$). The isosurface value is ± 0.05 au.

character. Close in energy is a degenerate pair of e symmetry π-type orbitals (labeled d_{π_1} and d_{π_2}) which also have primarily ruthenium $4d$ character. In the valence space, the pyridine orbitals transform according to the a_2 and e irreducible representations; however, there is no a_2 symmetry ruthenium $4d$ orbital. As a result, the lowest-unoccupied molecular orbital (LUMO) is a π^*-type orbital (labeled L^*) which is bonding between the pyridine ligands but otherwise has no interaction with the ruthenium. Close in energy to the LUMO is another pair of degenerate e symmetry π^*-type orbitals (labeled $L_{\pi_1^*}$ and $L_{\pi_2^*}$) which have mixed metal and ligand character. Similar frontier orbitals were found for the dye molecules RuP, RuP2, and RuP3 which can be found in Fig. S2-S5 of the supporting information.

Transitions between the frontier molecular orbitals account for nine singlet and 27 triplet

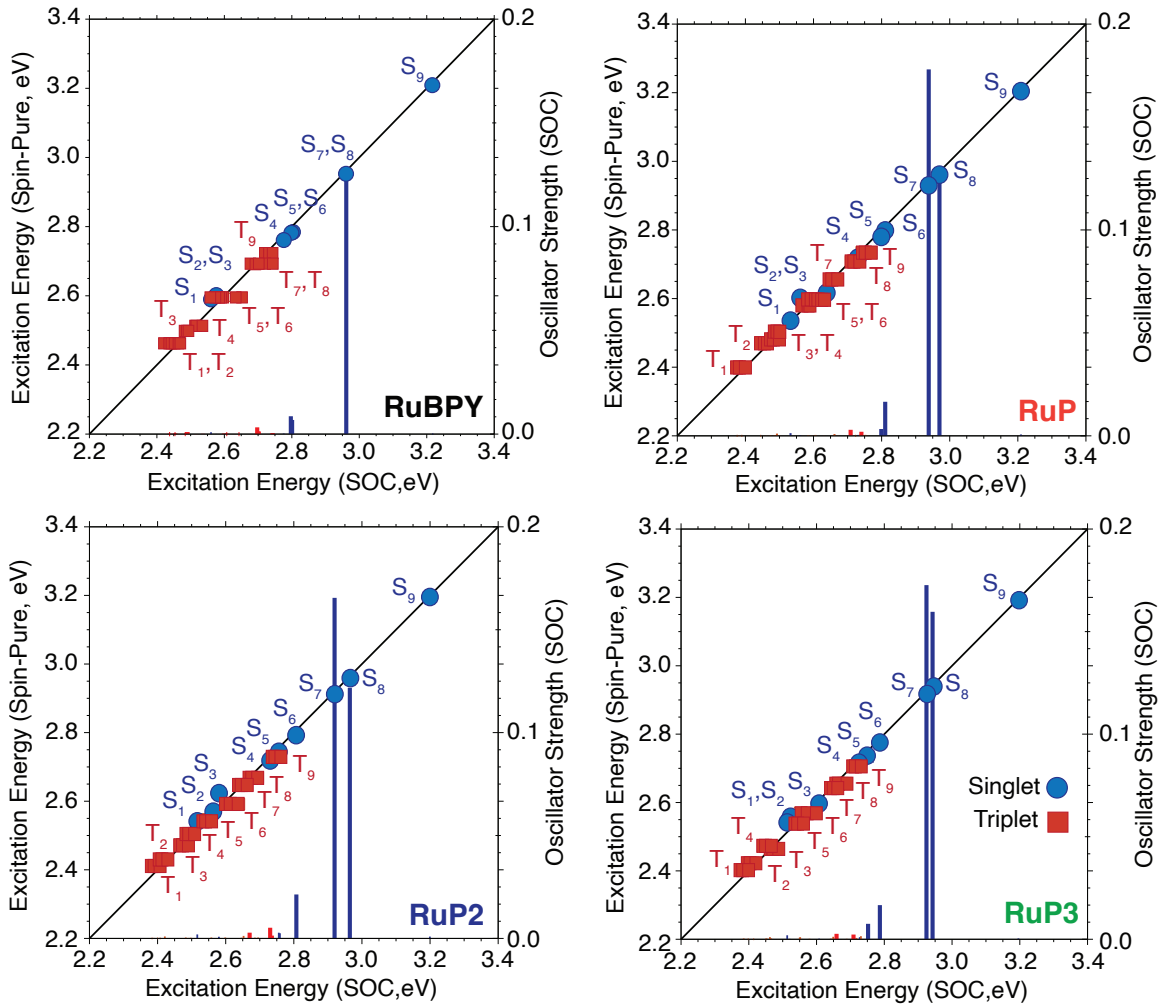

Figure 4: A comparison between the spin-pure excitation energies (y-axis) and the spin-orbit coupled excitation energies (x-axis) of the lowest nine singlet (blue circles) and 27 triplet states (red squares) evaluated at the ground-state optimized geometries. The excitation energy comparison of RuBPY (top left), RuP (top right), RuP2 (bottom left), and RuP3 (bottom right). All energies are in eV. The impulse plots correspond to the SOC corrected oscillator strengths with values shown on the y2-axis.

excited states which underlie the MLCT band. Comparisons between the spin-pure and SOC transition energies, evaluated at the optimized geometry of each dye molecule, are shown in Fig. 4. Although there are regions where the transition energies overlap (e.g. in the $2.5-2.8$ eV range), the triplet manifolds generally lies lower in energy than the singlet manifolds. The SOC oscillator strengths identify that weak transitions, S_5 and S_6, are present and the brightest transitions are S_7 and S_8 which is consistent for each dye molecule. For RuBPY

Table 1: A comparison between the SOC excitation energies (eV), oscillator strengths, percent characters, and assignments evaluated at the optimized geometries. The orbital excitation character ($|X_{ai}|^2$) is shown in the last two columns. The percent characters are defined as $d_\pi = d_{\pi_1} + d_{\pi_2}$ and $L_{\pi^*} = L_{\pi_1^*} + L_{\pi_2^*}$.

Peak	**Energy (eV)**	f_{osc}	P_T	P_S	$d_\pi \rightarrow L^*$	$d_\pi \rightarrow L_{\pi^*}$
RuBPY						
S_5	2.797	0.009	6%	94%	72%	25%
S_6	2.801	0.007	12%	88%	70%	25%
S_7	2.961	0.126	2%	98%	24%	72%
S_8	2.962	0.125	2%	98%	24%	72%
RuP						
S_5	2.799	0.003	11%	89%	37%	58%
S_6	2.810	0.016	5%	95%	53%	44%
S_7	2.938	0.178	2%	98%	32%	63%
S_8	2.970	0.123	2%	98%	13%	83%
RuP2						
S_5	2.756	0.003	42%	58%	37%	54%
T_9 (m=$\pm$1)	2.759	0.003	58%	42%	29%	59%
S_6	2.807	0.021	9%	91%	44%	52%
S_7	2.920	0.165	2%	98%	29%	66%
S_8	2.964	0.122	2%	98%	13%	82%
RuP3						
S_5	2.752	0.007	14%	86%	73%	23%
S_6	2.787	0.017	5%	95%	53%	44%
S_7	2.924	0.173	2%	98%	26%	69%
S_8	2.942	0.160	2%	98%	17%	78%

the bright transitions are degenerate, however breaking the symmetry with phosphonation splits these transitions in the other derivatives. The results are a slightly brighter S_7 and slightly weaker S_8 transition. At these geometries, the effect of SOC on the linear absorption is incredibly weak with negligible oscillator strengths attributed to direct singlet-to-triplet absorption.

A breakdown of the singlet/triplet and orbital excitation character of these transitions is provided in Table 1. Since the bright S_7 and S_8 transitions are well separated from the

triplet manifold, SOC is relatively weak with $P_S = 98\%$ for all the dye molecules. SOC is slightly stronger for the S_5 and S_6 transitions with triplet characters that range between 5% and 14% for RuBPY, RuP, and RuP3. Although the oscillator strength for the S_5 transition of RuP2 is relatively weak ($f_{osc} = 0.003$), there is a significant SOC which results from a near degeneracy with the T_9 ($m = \pm 1$, contributing equally each with 23% character) transitions. In general, the bright transitions are assigned to two types of orbital excitations. The S_7 and S_8 transitions are $d_\pi \rightarrow L_{\pi^*}$ excitations with percent characters ranging from 63%–83%. The weaker transitions, S_5 and S_6, have mixed $d_\pi \rightarrow L^*$ and $d_\pi \rightarrow L_{\pi^*}$ character with values ranging from 37% for S_5 in RuP and RuP2 to 72%–73% for RuBPY and RuP3. Interestingly, since the valence L_{π^*} orbitals contain significantly mixed metal *and* ligand character, the MLCT band is not simply constructed from metal-to-ligand transitions but is better described as metal-to-metal-ligand transitions.

Comparisons between the simulated and experimental linear absorption cross sections are shown in Fig. 5. After Wigner sampling of the vibrational degrees of freedom, a significant SOC contribution to the line shape is observed. The SOC contribution can be quantified by summing the singlet and triplet components independently, revealing that SOC accounts for $\approx 20\%$ of the total contribution which is consistent across all four dye molecules. Since many of the triplet states are lower in energy than the singlet states, the singlet contributions define the higher-energy region of the line shape, while the triplet contributions define the broader, lower-energy region. In general, the agreement between the simulations and experiments is quite good particularly in the lower-energy region of the band.

Although the lower energy line shape is defined by triplet contributions, the SOC correction to the linear absorption cross sections is greater in the intermediate region, as shown in the difference plots of Fig. 6. Here, a negative difference indicates a greater SOC correction. Generally, the SOC corrections for RuBPY and RuP3 are smaller compared to those for RuP and RuP2. At the lower and higher energy regions of the band, the differences are negative, indicating that SOC increases the linear absorption cross section. The SOC correction is

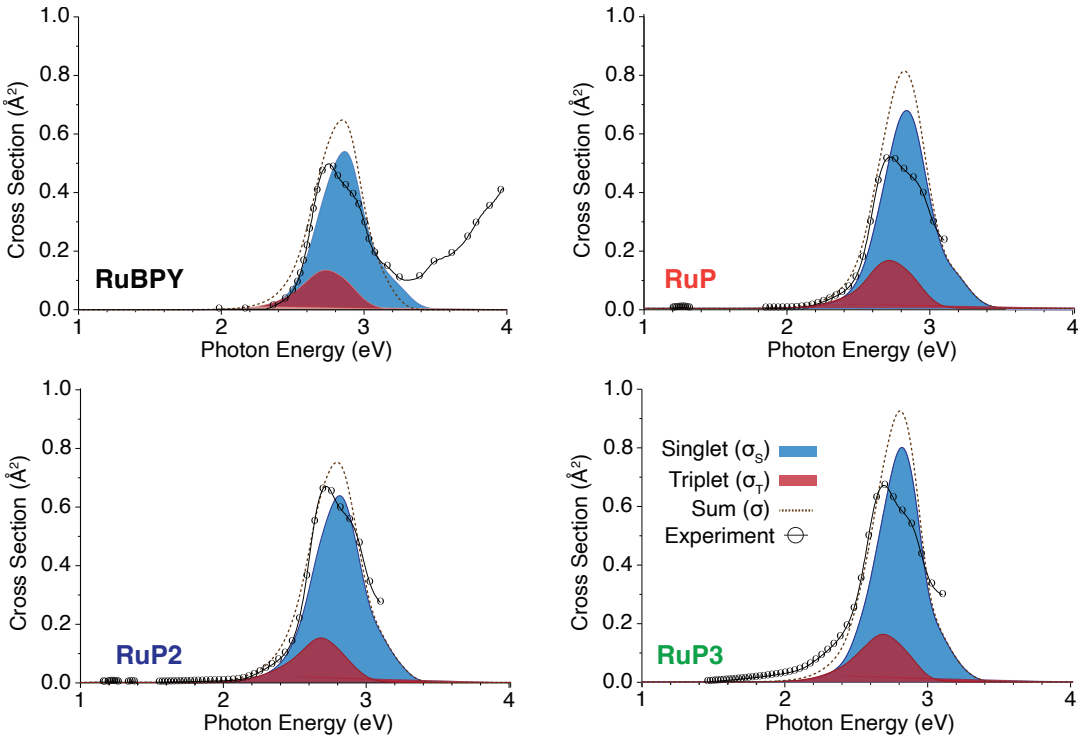

Figure 5: A comparison between the experimental and simulated linear absorption cross sections (Å^2) for RuBPY (top left), RuP (top right), RuP2 (bottom left) and RuP3 (bottom right). All energies are in (eV). The singlet (blue shaded) and triplet (red shaded) contributions are defined as $\sigma_S = P_S\sigma$ and $\sigma_T = P_T\sigma$. The dashed brown line is the sum of the singlet and triplet contributions. The experimental linear absorption cross sections are shown with open circles.

most significant for RuP and RuP2, occurring in the 2.8eV–2.9eV region, where the singlet and triplet manifolds overlap. In this region, the transition energies are significantly modulated by the vibrational degrees of freedom. The width of the difference cross section, which is a metric for the range of overlapping transitions, is broadest for RuP which suggests that SOC is greatest for this dye molecule.

The calculated intersystem crossing rate coefficients are presented in Table 2. The rate coefficients, out of each singlet state, were weighted by their respective normalized oscillator strengths (f_{osc}) reported in Table 1 and summed over the nine states in the triplet manifold. The $m = 0, \pm 1$ sub levels of the triplet states were included using Eq.17. For each dye molecule, the fastest intersystem crossing occurs out of the S_7 state where the most significant

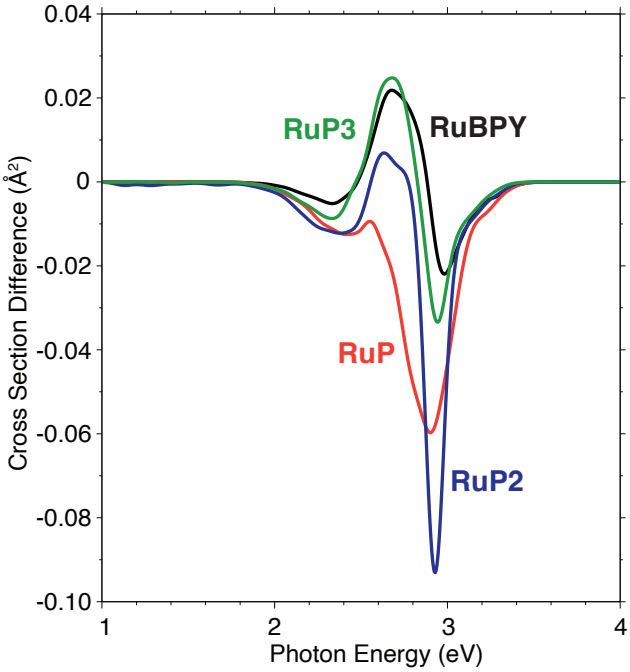

Figure 6: The difference between the spin-pure and SOC simulated linear absorption cross sections (Å^2) as a function of excitation energy (eV) for RuBPY (black), RuP (red), RuP2 (blue), and RuP3 (green).

Table 2: A comparison between the weighted sum of the intersystem crossing rate coefficients (s^{-1}) from each excited singlet state (S_I) into each state in the triplet manifold. The total intersystem crossing rate coefficient (Total) is the sum of each column.

k_{ISC}	RuBPY	RuP	RuP2	RuP3
$S_5 \rightarrow T_J$	3.07E+12	2.49E+12	1.19E+12	2.44E+12
$S_6 \rightarrow T_J$	2.83E+12	4.57E+12	6.09E+12	3.61E+12
$S_7 \rightarrow T_J$	9.79E+12	2.18E+13	1.46E+13	6.61E+12
$S_8 \rightarrow T_J$	1.31E+12	5.93E+12	1.12E+13	5.70E+12
Total	1.70E+13	3.48E+13	3.31E+13	1.84E+13

coefficients are $k_{ISC} = 2.18 \times 10^{13}$ s^{-1} for RuP and $k_{ISC} = 1.46 \times 10^{13}$ s^{-1} for RuP2. Although one might expect the fastest crossing from S_5 and S_6 since they are closer in energy to the triplet states and have a greater SOC, the much weaker oscillator strength inhibits intersystem crossing from these states. The total intersystem crossing rate coefficients (Total) are, however, predicted to happen ultrafast with rate coefficients on the order of 10^{13} s^{-1}

for each dye molecule. The rate coefficients are slightly faster for RuP and RuP2 which is consistent with the greater SOC in the overlapping regions of the linear absorption spectrum. A state-specific table of the weighted rate coefficients is provided in Table S3 of the supporting information.

For each dye molecule, the fastest intersystem crossing rate coefficients were found to occur out of the S_7 state. According to the rate coefficients in Table S3, the intersystem crossing can be mostly attributed to single transitions. An analysis of the natural transition orbitals (NTOs) underlying these transitions is presented in Fig. 7. The NTOs for the S_7 state identify two primary orbital contributions which account for greater than 98% of each transition. The corresponding orbital contributions have $d_{\pi_1} \rightarrow L_{\pi_1^*}$ and a $d_{\pi_2} \rightarrow L_{\pi_2^*}$ character. For RuBPY, RuP, and RuP3 the final triplet state is T_3 which correspond to a single NTO pair with $4d_{z^2} \rightarrow L_{\pi_2^*}$ character. For RuP2, the final triplet state also corresponds to a single NTO pair, however this pair is T_1 with $4d_{z^2} \rightarrow L_{\pi_1^*}$ character. The fastest intersystem crossing rate coefficients correspond to excitations that differ by a single occupied NTO. For the triplet state this is the highest-occupied $4d_{z^2}$ and for the singlet state this is the d_{π_1} NTO. This result can be explained since the BP Hamiltonian is a sum of 1-electron operators and Slater-Condon rules indicate that this 1-electron operator can only couple together determinants that differ by a single spin orbital.

The intersystem crossing rate coefficients reported here are in excellent agreement with the kinetics analysis of the spectroscopy that we presented in Ref. 61. In that work, we extracted intersystem rate coefficients $k_{ISC} = 4.0 \times 10^{13}$ s^{-1} for RuP and RuP2 and $k_{ISC} = 2.0 \times 10^{13}$ s^{-1} for RuP3 which clearly have the same magnitude and even follow the same trend as the rate coefficients reported in this work. However, unlike the sums of exponentials analysis that was performed in Ref. 54, the rate coefficients reported in the kinetics analysis in Ref. 61 correspond cleanly to a mechanism. In that study, the simplest possible assumption was made that the singlet-to-triplet intersystem crossing involved one primary singlet state. Treating the closely spaced transitions S_7 and S_8 as one, the present study

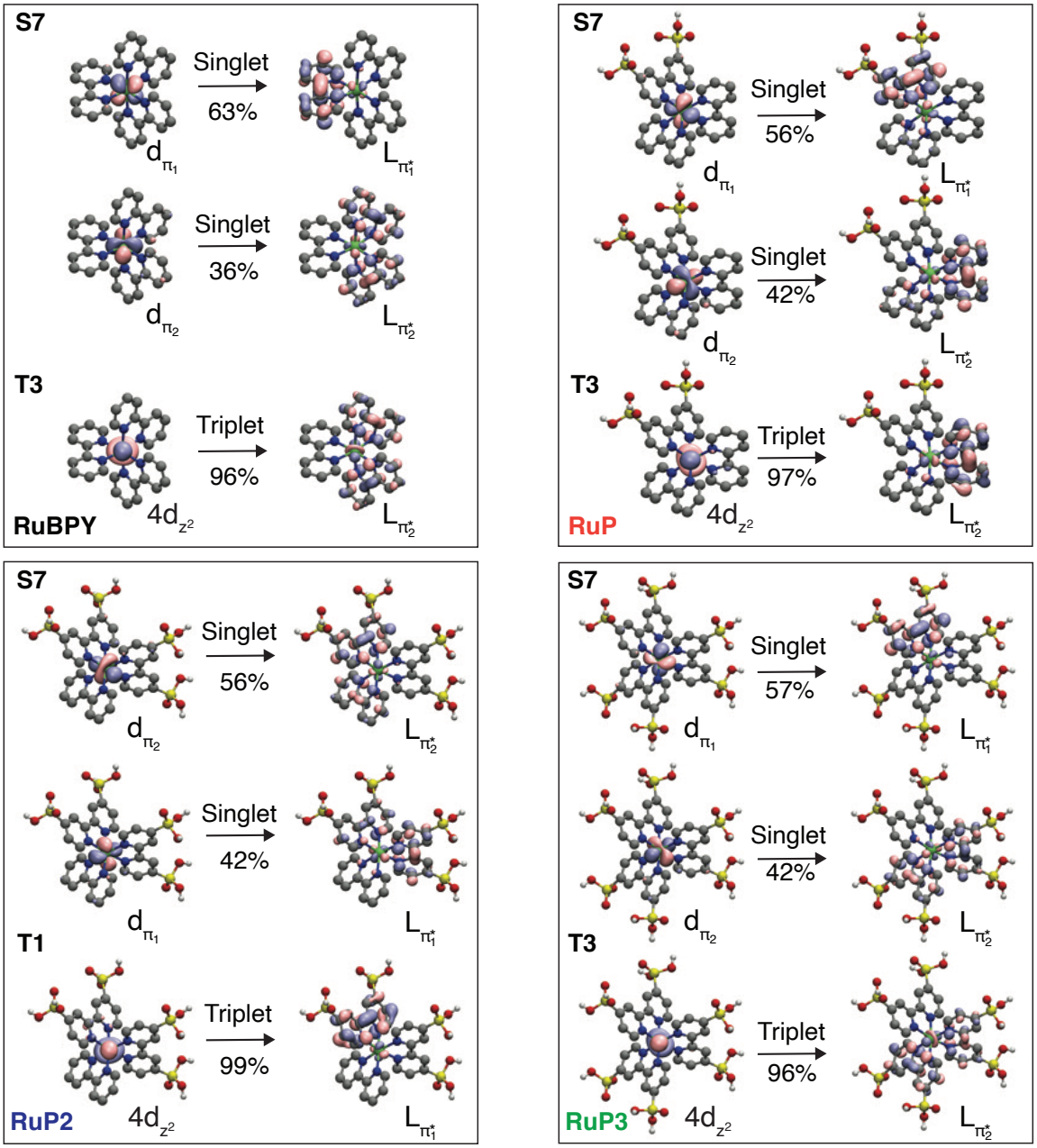

Figure 7: The natural transition orbitals with assignments for the fastest intersystem crossing transitions in RuBPY (top left), RuP (top right), RuP2 (bottom left), and RuP3 (bottom right). The rate coefficients correspond to transitions from $d_\pi \rightarrow L_{\pi^*}$ singlet states into $4d_{z^2} \rightarrow L_{\pi^*}$ triplet states. The percent character for each natural transition orbital pair is shown below the arrows. The isosurface value is ± 0.05 au.

supports that assumption, and also reveals that the ultrafast intersystem crossing can be assigned to transitions between occupied $4d_{z^2}$ and d_{π_1} orbitals. The magnitudes reported here also support our previous conclusion in Ref. 61 that a second process—ultrafast nonra-

diative relaxation back to the ground state—is competitive with intersystem crossing which we needed to invoke in order to have quantitative agreement with the spectral data. On the basis of early studies[103] it is widely assumed that intersystem crossing is 100% efficient, however we found that this is only true when the dye is supported on a solid.

Conclusions

In this work, TDDFT/TDA and the perturbation theory was employed to study the effects that SOC has on the absorption cross sections and intersystem crossing rate coefficients of a set of ruthenium polypyridyl dye molecules (RuBPY, RuP, RuP2, and RuP3). While at the optimized ground-state geometries SOC was found to have a negligible effect on the transition energies and oscillator strengths, two transitions S_7 and S_8 were identified which carried significant oscillator strength. The SOC was found to have a negligible effect on these transitions since they are well separated from the triplet manifold. Although it may be expected that the MLCT band is defined by metal-to-ligand transitions, an analysis of the electronic structure of the excited states suggests that the valence orbitals contain both metal *and* ligand character. The analysis presented here identified that this mixed character is significant throughout many of the excited states.

When sampling electronic transitions from the vibrational degrees of freedom, the simulations identified a significant SOC effect on the MLCT line shapes. Comparisons were made in Fig. 5 between the experimental and simulated linear absorption cross sections which were generally in good agreement. The simulated cross sections were decomposed into singlet and triplet contributions which revealed that SOC has a nearly 20% contribution to the overall line shape. Additionally, the difference cross sections revealed that the SOC correction was greatest for RuP with a broad difference line shape which indicates significant overlap with transitions from the triplet manifold. The SOC correction to the cross sections for RuBPY and RuP3 were found to be much less significant in comparison.

Finally, the intersystem crossing rate coefficients were analyzed and found to occur within 10^{13} s^{-1} for each dye molecule in good agreement with rate coefficients extracted from spectroscopic data using a kinetics analysis. The intersystem crossing rate coefficient corresponding to the fastest singlet-to-triplet transitions were identified and the corresponding natural transition orbitals were analyzed. We found that the fastest transitions occur between singlet and triplet states that differ by a single spin orbital. Although the simple analysis provided reasonable intersystem crossing rate coefficients for these dyes, explicit dynamic effects such as anharmonicity and nonadiabaticity were ignored in these models. An area of future direction will be to incorporate the effects of SOC into some of our recent TDDFT/TDA quasi-classical molecular dynamics approaches.[104] The calculations reported here were on gas phase molecules and in condensed phase other perturbations can accelerate these transitions. Another area of future direction will be to incorporate condensed phase effects (e.g. using polarizable continuum models)[105] into these calculations.

Associated Content

The supporting information provides effective nuclear charges used in the BP Hamiltonian, definitions employed in the kinetics model, a table of the state-specific intersystem crossing rate coefficients, and some additional orbital, vibrational structure, SOC, and transition analysis (pdf). The mode-specific reorganization energies, driving forces, and spin-orbit coupling constants are provided (xlsx). Cartesian coordinates at the minimum energy geometries on the ground and excited electronic states of RuBPY, RuP, RuP2, and RuP3 are also provided (xyz).

Acknowledgments

The theory development, data analysis, and computations for this work were performed by J.J.T, S.J.C, and M.H-G, supported by the National Science Foundation under grant number

CHE-1856707. J.J.T., T.P.C, F.A.H, and M.H-G. acknowledge additional support from the Director, Office of Science, Office of Basic Energy Sciences of the U.S. Department of Energy under contract No. DE-AC02-05CH11231. T.P.C, F.A.H, and M.H-G. conceptualized the project. T.P.C. and F.A.H. performed the initial dye photophysical kinetics simulations, contributed knowledge of the relationship between absorption and kinetics to frame the project, and supported understanding the implications of the results, with support from the U.S. Department of Energy Chemical Sciences, Geosciences, and Biosciences Division, in the Solar Photochemistry Program. This research used resources from the National Energy Research Scientific Computing Center (NERSC), a U.S. Department of Energy Office of Science User Facility located at Lawrence Berkeley National Laboratory, operated under Contract No. DE-AC02-05CH11231 using NERSC award BES-ERCAP0029035.

References

(1) Grätzel, M. Dye–Sensitized Solar Cells. *J. Photochem. Photobiol. C: Photochem. Rev.* **2003**, *4*, 145–153.

(2) Gong, J.; Sumathy, K.; Qiao, Q.; Zhou, Z. Review on Dye–Sensitized Solar Cells (DSSCs): Advanced Techniques and Research Trends. *Renew. Sust. Energ. Rev.* **2017**, *68*, 234–246.

(3) Mozaffari, S.; Nateghi, M. R.; Zarandi, M. B. An Overview of the Challenges in the Commercialization of Dye Sensitized Solar Cells. *Renew. Sustain. Energy Rev.* **2017**, *71*, 675–686.

(4) House, R. L.; Iha, N. Y. M.; Coppo, R. L.; Alibabaei, L.; Sherman, B. D.; Kang, P.; Brennaman, M. K.; Hoertz, P. G.; Meyer, T. J. Artificial Photosynthesis: Where are we now? Where can we go? *J. Photochem. Photobio* **2015**, *25*, 32–45.

(5) Yun, S.; Vlachopoulos, N.; Qurashi, A.; Ahmad, S.; Hagfeldt, A. Dye Sensitized Photoelectrolysis Cells. *Chem. Soc. Rev.* **2019**, *48*, 3705–3722.

(6) Gibson, E. A. Dye–Sensitized Photocathodes for H_2 Evolution. *Chem. Soc. Rev.* **2017**, *46*, 6194–6209.

(7) Brennaman, M. K.; Dillon, R. J.; Alibabaei, L.; Gish, M. K.; Dares, C. J.; Ashford, D. L.; House, R. L.; Meyer, G. J.; Papanikolas, J. M.; Meyer, T. J. Finding the way to Solar Fuels with Dye-Sensitized Photoelectrosynthesis Cells. *J. Am. Chem. Soc.* **2016**, *138*, 13085–13102.

(8) Alibabaei, L.; Luo, H.; House, R. L.; Hoertz, P. G.; Lopez, R.; Meyer, T. J. Applications of Metal Oxide Materials in Dye Sensitized Photoelectrosynthesis Cells for Making Solar Fuels: Let the Molecules do the Work. *J. Mat. Chem. A* **2013**, *1*, 4133–4145.

(9) Zeng, K.; Tong, Z.; Ma, L.; Zhu, W.-H.; Wu, W.; Xie, Y. Molecular Engineering Strategies for Fabricating Efficient Porphyrin–Based Dye–Sensitized Solar Cells. *Energy Environ. Sci.* **2020**, *13*, 1617–1657.

(10) Nazeeruddin, M. K.; Klein, C.; Liska, P.; Grätzel, M. Synthesis of Novel Ruthenium Sensitizers and their Application in Dye–Sensitized Solar Cells. *Coord. Chem. Rev.* **2005**, *249*, 1460–1467.

(11) Sharma, K.; Sharma, V.; Sharma, S. Dye–Sensitized Solar Cells: Fundamentals and Current Status. *Nanoscale Res. Lett.* **2018**, *13*, 1–46.

(12) Cooper, C. B. et al. Design–to–Device Approach Affords Panchromatic Co-Sensitized Solar Cells. *Adv. Energy Mater.* **2019**, *9*, 1802820.

(13) James, S.; Contractor, R. Study on Nature-Inspired Fractal Design–Based Flexible

Counter Electrodes for Dye–Sensitized Solar Cells Fabricated Using Additive Manufacturing. *Sci. Rep.* **2018**, *8*, 17032.

(14) Freitag, M.; Teuscher, J.; Saygili, Y.; Zhang, X.; Giordano, F.; Liska, P.; Hua, J.; Zakeeruddin, S. M.; Moser, J.-E.; Grätzel, M.; Hagfeldt, A. Dye–Sensitized Solar Cells for Efficient Power Generation Under Ambient Lighting. *Nat. Photonics* **2017**, *11*, 372–378.

(15) Muñoz-García, A. B.; Benesperi, I.; Boschloo, G.; Concepcion, J. J.; Delcamp, J. H.; Gibson, E. A.; Meyer, G. J.; Pavone, M.; Pettersson, H.; Hagfeldt, A.; Freitag, M. Dye–Sensitized Solar Cells Strike Back. *Chem. Soc. Rev.* **2021**, *50*, 12450–12550.

(16) Alhorani, S.; Kumar, S.; Genwa, M.; Meena, P. Review of Latest Efficient Sensitizer in Dye–Sensitized Solar Cells. AIP Conf. 2020.

(17) Kokkonen, M.; Talebi, P.; Zhou, J.; Asgari, S.; Soomro, S. A.; Elsehrawy, F.; Halme, J.; Ahmad, S.; Hagfeldt, A.; Hashmi, S. G. Advanced Research Trends in Dye–Sensitized Solar Cells. *J. Mater. Chem. A* **2021**, *9*, 10527–10545.

(18) Samanta, P. N.; Majumdar, D.; Roszak, S.; Leszczynski, J. First–Principles Approach for Assessing Cold Electron Injection Efficiency of Dye–Sensitized Solar Cell: Elucidation of Mechanism of Charge Injection and Recombination. *J. Phys. Chem. C* **2020**, *124*, 2817–2836.

(19) Janjua, M. R. S. A.; Khan, M. U.; Khalid, M.; Ullah, N.; Kalgaonkar, R.; Alnoaimi, K.; Baqader, N.; Jamil, S. Theoretical and Conceptual Framework to Design Efficient Dye–Sensitized Solar Cells (DSSCs): Molecular Engineering by DFT Method. *J. Clust. Sci.* **2021**, *32*, 243–253.

(20) Xu, Y.; Xu, X.; Li, M.; Lu, W. Prediction of Photoelectric Properties, Especially Power Conversion Efficiency of Cells, of IQ1 and Derivative Dyes in High–Efficiency Dye–Sensitized Solar Cells. *Solar Energy* **2020**, *195*, 82–88.

(21) Cole, J. M.; Pepe, G.; Al Bahri, O. K.; Cooper, C. B. Cosensitization in Dye–Sensitized Solar Cells. *Chem. Rev.* **2019**, *119*, 7279–7327.

(22) Hagfeldt, A.; Boschloo, G.; Sun, L.; Kloo, L.; Pettersson, H. Dye–Sensitized Solar Cells. *Chem. Rev.* **2010**, *110*, 6595–6663.

(23) He, S.; Lan, Z.; Zhang, B.; Gao, Y.; Shang, L.; Yue, G.; Chen, S.; Shen, Z.; Tan, F.; Wu, J. Holistically Optimizing Charge Carrier Dynamics Enables High–Performance Dye–Sensitized Solar Cells and Photodetectors. *ACS Appl. Mater. Interfaces.* **2022**, *14*, 43576–43585.

(24) Robertson, N. Optimizing Dyes for Dye–Sensitized Solar Cells. *Angew. Chem., Int. Ed.* **2006**, *45*, 2338–2345.

(25) Baby, R.; Nixon, P. D.; Kumar, N. M.; Subathra, M.; Ananthi, N. A Comprehensive Review of Dye-Sensitized Solar Cell Optimal Fabrication Conditions, Natural Dye Selection, and Application-Based Future Perspectives. *Environ. Sci. Pollut. Res.* **2022**, 1–34.

(26) Le Bahers, T.; Labat, F.; Pauporté, T.; Lainé, P. P.; Ciofini, I. Theoretical Procedure for Optimizing Dye–Sensitized Solar Cells: from Electronic Structure to Photovoltaic Efficiency. *J. Am. Chem. Soc.* **2011**, *133*, 8005–8013.

(27) Nabil, E.; Hasanein, A. A.; Alnoman, R. B.; Zakaria, M. Optimizing the Cosensitization Effect of SQ02 Dye on BP–2 Dye–Sensitized Solar Cells: a Computational Quantum Chemical Study. *J. Chem. Inf. Model.* **2021**, *61*, 5098–5116.

(28) Heng, P.; An, B.; Ren, H.; Hu, Y.; Guo, X.; Mao, L.; Wang, L.; Zhang, J. Influence of Different Molecular Design Strategies on Photovoltaic Properties of a Series of Triphenylamine–Based Organic Dyes for Dye–Sensitized Solar Cells: Insights from Theoretical Investigations. *J. Phys. Chem. C.* **2020**, *124*, 15036–15044.

(29) De Angelis, F. Modeling Materials and Processes in Hybrid/Organic Photovoltaics: From Dye–Sensitized to Perovskite Solar Cells. *Acc. Chem. Res.* **2014**, *47*, 3349–3360.

(30) Pastore, M.; Fantacci, S.; De Angelis, F. Modeling Excited States and Alignment of Energy Levels in Dye–Sensitized Solar Cells: Successes, Failures, and Challenges. *J. Phys. Chem. C.* **2013**, *117*, 3685–3700.

(31) Kim, J.; Kang, D.-g.; Kim, S. K.; Joo, T. Role of Coherent Nuclear Motion in the Ultrafast Intersystem Crossing of Ruthenium Complexes. *Phys. Chem. Chem. Phys.* **2020**, *22*, 25811–25818.

(32) Yoon, S.; Kukura, P.; Stuart, C. M.; Mathies, R. A. Direct Observation of the Ultrafast Intersystem Crossing in tris(2,2'–bipyridine) ruthenium (II) Using Femtosecond Stimulated Raman Spectroscopy. *Mol. Phys.* **2006**, *104*, 1275–1282.

(33) Bhasikuttan, A. C.; Suzuki, M.; Nakashima, S.; Okada, T. Ultrafast Fluorescence Detection in Tris(2,2'–bipyridine) ruthenium (II) Complex in Solution: Relaxation Dynamics Involving Higher Excited States. *J. Am. Chem. Soc.* **2002**, *124*, 8398–8405.

(34) Kober, E. M.; Meyer, T. J. Concerning the Absorption Spectra of the Ions M $(bpy)_3{}^{2+}$ (M= Fe, Ru, Os; bpy= 2, 2'–bipyridine). *Inorg. Chem.* **1982**, *21*, 3967–3977.

(35) Kawamoto, K.; Tamiya, Y.; Storr, T.; Cogdell, R. J.; Kinoshita, I.; Hashimoto, H. Disentangling the 1MLCT Transition of $[Ru(bpy)_3]^{2+}$ by Stark Absorption Spectroscopy. *J. Photochem. Photobiol., A* **2018**, *353*, 618–624.

(36) Dongare, P.; Myron, B. D.; Wang, L.; Thompson, D. W.; Meyer, T. J. $[Ru(bpy)_3]^{2+*}$ Revisited. Is it Localized or Delocalized? How Does it Decay? *Coord. Chem. Rev.* **2017**, *345*, 86–107.

(37) Zeng, C.; Li, Y.; Zheng, H.; Ren, M.; Wu, W.; Chen, Z. Nature of Ultrafast Dynamics

in the Lowest–Lying Singlet Excited State of $[Ru(bpy)_3]^{2+}$. *Phys. Chem. Chem. Phys.* **2024**,

(38) Kitzmann, W. R.; Heinze, K. Charge–Transfer and Spin–Flip States: Thriving as Complements. *Angew. Chem. Int. Ed.* **2023**, *62*, e202213207.

(39) Martirez, J. M. P.; Carter, E. A. Metal–to–ligand Charge–Transfer Spectrum of a Ru–Bipyridine–Sensitized TiO_2 Cluster from Embedded Multiconfigurational Excited-State Theory. *J. Phys. Chem. A* **2021**, *125*, 4998–5013.

(40) Tavernelli, I.; Curchod, B. F.; Rothlisberger, U. Nonadiabatic Molecular Dynamics with Solvent Effects: A LR–TDDFT QM/MM Study of Ruthenium (II) tris(bipyridine) in Water. *Chem. Phys.* **2011**, *391*, 101–109.

(41) Grotjahn, R.; Kaupp, M. Reliable TDDFT Protocol Based on a Local Hybrid Functional for the Prediction of Vibronic Phosphorescence Spectra Applied to Tris(2,2'–bipyridine)–Metal Complexes. *J. Phys. Chem. A* **2021**, *125*, 7099–7110.

(42) Munshi, M. U.; Martens, J.; Berden, G.; Oomens, J. Vibrational Spectra of the Ruthenium–Tris–Bipyridine Dication and its Reduced Form in Vacuo. *J. Phys. Chem. A* **2020**, *124*, 2449–2459.

(43) Thompson, D. W.; Ito, A.; Meyer, T. J. $[Ru(bpy)_3]^{2+*}$ and Other Remarkable Metal–to–Ligand Charge Transfer (MLCT) Excited States. *Pure Appl. Chem.* **2013**, *85*, 1257–1305.

(44) Heindl, M.; Hongyan, J.; Hua, S.-A.; Oelschlegel, M.; Meyer, F.; Schwarzer, D.; González, L. Excited–State Dynamics of $[Ru(S–Sbpy)(bpy)_2]^{2+}$ to Form Long–Lived Localized Triplet States. *Inorg. Chem.* **2021**, *60*, 1672–1682.

(45) Neale, N. R.; Pekarek, R. T. *Springer Handbook of Inorganic Photochemistry*; Springer, 2022; pp 923–964.

(46) Ashford, D. L.; Gish, M. K.; Vannucci, A. K.; Brennaman, M. K.; Templeton, J. L.; Papanikolas, J. M.; Meyer, T. J. Molecular Chromophore–Catalyst Assemblies for Solar Fuel Applications. *Chem. Rev.* **2015**, *115*, 13006–13049.

(47) Hanson, K.; Brennaman, M. K.; Ito, A.; Luo, H.; Song, W.; Parker, K. A.; Ghosh, R.; Norris, M. R.; Glasson, C. R.; Concepcion, J. J.; Lopez, R.; Meyer, T. J. Structure–Property Relationships in Phosphonate–Derivatized, Ru^{II} Polypyridyl Dyes on Metal Oxide Surfaces in an Aqueous Environment. *J. Phys. Chem. C* **2012**, *116*, 14837–14847.

(48) Giokas, P. G.; Miller, S. A.; Hanson, K.; Norris, M. R.; Glasson, C. R.; Concepcion, J. J.; Bettis, S. E.; Meyer, T. J.; Moran, A. M. Spectroscopy and Dynamics of Phosphonate–Derivatized Ruthenium Complexes on TiO_2. *J. Phys. Chem. C* **2013**, *117*, 812–824.

(49) Pashaei, B.; Shahroosvand, H.; Graetzel, M.; Nazeeruddin, M. K. Influence of Ancillary Ligands in Dye–Sensitized Solar Cells. *Chem. Rev.* **2016**, *116*, 9485–9564.

(50) Meng, S.; Kaxiras, E.; Nazeeruddin, M. K.; Grätzel, M. Design of Dye Acceptors for Photovoltaics from First–Principles Calculations. *J. Phys. Chem. C* **2011**, *115*, 9276–9282.

(51) Lin, C.; Liu, Y.; Wang, G.; Li, K.; Xu, H.; Zhang, W.; Shao, C.; Yang, Z. Novel Dyes Design Based on First Principles and the Prediction of Energy Conversion Efficiencies of Dye–Sensitized Solar Cells. *ACS Omega* **2020**, *6*, 715–722.

(52) Atkins, A. J.; Talotta, F.; Freitag, L.; Boggio-Pasqua, M.; González, L. Assessing Excited State Energy Gaps with Time-Dependent Density Functional Theory on Ru(II) Complexes. *J. Chem. Theory Comput.* **2017**, *13*, 4123–4145.

(53) Cheshire, T. P.; Boodry, J.; Kober, E. A.; Brennaman, M. K.; Giokas, P. G.; Zigler, D. F.; Moran, A. M.; Papanikolas, J. M.; Meyer, G. J.; Meyer, T. J.;

Houle, F. A. A Quantitative Model of Charge Injection by Ruthenium Chromophores Connecting Femtosecond to Continuous Irradiance Conditions. *J. Chem. Phys.* **2022**, *157*.

(54) Zigler, D. F.; Morseth, Z. A.; Wang, L.; Ashford, D. L.; Brennaman, M. K.; Grumstrup, E. M.; Brigham, E. C.; Gish, M. K.; Dillon, R. J.; Alibabaei, L.; others Disentangling the Physical Processes Responsible for the Kinetic Complexity in Interfacial Electron Transfer of Excited Ru(II) Polypyridyl Dyes on TiO_2. *J. Am. Chem. Soc.* **2016**, *138*, 4426–4438.

(55) Atkins, A. J.; González, L. Trajectory Surface–Hopping Dynamics Including Intersystem Crossing in $[Ru(bpy)_3]^{2+}$. *J. Phys. Chem. Lett.* **2017**, *8*, 3840–3845.

(56) Talbot, J. J.; Arias-Martinez, J. E.; Cotton, S. J.; Head-Gordon, M. Fantastical Excited State Optimized Structures and Where to Find Them. *J. Chem. Phys.* **2023**, *159*.

(57) Brown, A. M.; McCusker, C. E.; Carey, M. C.; Blanco-Rodríguez, A. M.; Towrie, M.; Clark, I. P.; Vlcek, A.; McCusker, J. K. Vibrational Relaxation and Redistribution Dynamics in Ruthenium (II) Polypyridyl-Based Charge–Transfer Excited States: A Combined Ultrafast Electronic and Infrared Absorption Study. *J. Phys. Chem. A* **2018**, *122*, 7941–7953.

(58) Borgwardt, M.; Wilke, M.; Kiyan, I. Y.; Aziz, E. F. Ultrafast Excited States Dynamics of $[Ru(bpy)_3]^{2+}$ dissolved in ionic liquids. *Phys. Chem. Chem. Phys.* **2016**, *18*, 28893–28900.

(59) Stark, C. W.; Schreier, W. J.; Lucon, J.; Edwards, E.; Douglas, T.; Kohler, B. Interligand Electron Transfer in Heteroleptic Ruthenium (II) Complexes Occurs on Multiple Time Scales. *J. Phys. Chem. A* **2015**, *119*, 4813–4824.

(60) Malone, R.; Kelley, D. Interligand Electron Transfer and Transition State Dynamics in Ru (II) Trisbipyridine. *J. Chem. Phys.* **1991**, *95*, 8970–8976.

(61) Cheshire, T. P.; Brennaman, M. K.; Giokas, P. G.; Zigler, D. F.; Moran, A. M.; Papanikolas, J. M.; Meyer, G. J.; Meyer, T. J.; Houle, F. A. Ultrafast Relaxations in Ruthenium Polypyridyl Chromophores Determined by Stochastic Kinetics Simulations. *J. Phys. Chem. B* **2020**, *124*, 5971–5985.

(62) Cheshire, T. P.; Houle, F. A. Ruthenium Dye Excitations and Relaxations in Natural Sunlight. *J. Phys. Chem. A* **2021**, *125*, 4365–4372.

(63) Damrauer, N. H.; Cerullo, G.; Yeh, A.; Boussie, T. R.; Shank, C. V.; McCusker, J. K. Femtosecond Dynamics of Excited-State Evolution in $[Ru(bpy)_3]^{2+}$. *Science* **1997**, *275*, 54–57.

(64) Yeh, A. T.; Shank, C. V.; McCusker, J. K. Ultrafast Electron Localization Dynamics Following Photo–Induced Charge Transfer. *Science* **2000**, *289*, 935–938.

(65) Cannizzo, A.; van Mourik, F.; Gawelda, W.; Zgrablic, G.; Bressler, C.; Chergui, M. Broadband Femtosecond Fluorescence Spectroscopy of $[Ru(bpy)_3]^{2+}$. *Angew. Chem., Int. Ed. Engl.* **2006**, *45*, 3174.

(66) Fedorov, D. G.; Koseki, S.; Schmidt, M. W.; Gordon, M. S. Spin–Orbit Coupling in Molecules: Chemistry Beyond the Adiabatic Approximation. *Int. Rev. Phys. Chem.* **2003**, *22*, 551–592.

(67) Knecht, S.; Repisky, M.; Jensen, H. J. A.; Saue, T. Exact Two–Component Hamiltonians for Relativistic Quantum Chemistry: Two–Electron Picture–Change Corrections Made Simple. *J. Chem. Phys.* **2022**, *157*.

(68) Sharma, P.; Jenkins, A. J.; Scalmani, G.; Frisch, M. J.; Truhlar, D. G.; Gagliardi, L.;

Li, X. Exact–Two–Component Multiconfiguration Pair–Density Functional Theory. *J. Chem. Theory Comput.* **2022**, *18*, 2947–2954.

(69) Lu, L.; Hu, H.; Jenkins, A. J.; Li, X. Exact–Two–Component Relativistic Multireference Second–Order Perturbation Theory. *J. Chem. Theory Comput.* **2022**, *18*, 2983–2992.

(70) Liu, W.; Peng, D. Exact Two–Component Hamiltonians Revisited. *J. Chem. Phys.* **2009**, *131*.

(71) Cunha, L. A.; Hait, D.; Kang, R.; Mao, Y.; Head-Gordon, M. Relativistic Orbital–Optimized Density Functional Theory for Accurate Core–Level Spectroscopy. *J. Phys. Chem. Lett.* **2022**, *13*, 3438–3449.

(72) Nakajima, T.; Hirao, K. The Douglas–Kroll–Hess Approach. *Chem. Rev.* **2012**, *112*, 385–402.

(73) Reiher, M. Douglas–Kroll–Hess Theory: a Relativistic Electrons–Only Theory for Chemistry. *Theor. Chem. Acc.* **2006**, *116*, 241–252.

(74) Van Lenthe, E. v.; Snijders, J.; Baerends, E. The Zero–Order Regular Approximation for Relativistic Effects: The Effect of Spin–Orbit Coupling in Closed Shell Molecules. *J. Chem. Phys.* **1996**, *105*, 6505–6516.

(75) Autschbach, J.; Ziegler, T. Nuclear Spin–Spin Coupling Constants from Regular Approximate Relativistic Density Functional Calculations. II. Spin–Orbit Coupling Effects and Anisotropies. *J. Chem. Phys.* **2000**, *113*, 9410–9418.

(76) Konecny, L.; Kadek, M.; Komorovsky, S.; Ruud, K.; Repisky, M. Resolution–of–Identity Accelerated Relativistic Two–and Four–Component Electron Dynamics Approach to Chiroptical Spectroscopies. *J. Chem. Phys.* **2018**, *149*.

(77) De Souza, B.; Farias, G.; Neese, F.; Izsak, R. Predicting Phosphorescence Rates of Light Organic Molecules Using Time–Dependent Density Functional Theory and the Path Integral Approach to Dynamics. *J. Chem. Theory Comput.* **2019**, *15*, 1896–1904.

(78) Hu, H.; Jenkins, A. J.; Liu, H.; Kasper, J. M.; Frisch, M. J.; Li, X. Relativistic Two–Component Multireference Configuration Interaction Method with Tunable Correlation Space. *J. Chem. Theory Comput.* **2020**, *16*, 2975–2984.

(79) Malmqvist, P. Å.; Roos, B. O.; Schimmelpfennig, B. The Restricted Active Space (RAS) State Interaction Approach with Spin–Orbit Coupling. *Chem. Phys. Lett.* **2002**, *357*, 230–240.

(80) Ganyushin, D.; Neese, F. A Fully Variational Spin–Orbit Coupled Complete Active Space Self–Consistent Field Approach: Application to Electron Paramagnetic Resonance G–Tensors. *J. Chem. Phys.* **2013**, *138*.

(81) Mai, S.; Müller, T.; Plasser, F.; Marquetand, P.; Lischka, H.; González, L. Perturbational Treatment of Spin–Orbit Coupling for Generally Applicable High–Level Multi–Reference Methods. *J. Chem. Phys.* **2014**, *141*.

(82) Marian, C. M. Spin–Orbit Coupling in Molecules. *Rev. Comput. Chem.* **2001**, *17*, 99–204.

(83) Kotaru, S.; Pokhilko, P.; Krylov, A. I. Spin–Orbit Couplings Within Spin-Conserving and Spin-Flipping Time-Dependent Density Functional Theory: Implementation and Benchmark Calculations. *J. Chem. Phys.* **2022**, *157*.

(84) Van Yperen-De Deyne, A.; Pauwels, E.; Van Speybroeck, V.; Waroquier, M. Accurate Spin–Orbit and Spin–Other–Orbit Contributions to the G–Tensor for Transition Metal Containing Systems. *Phys. Chem. Chem. Phys.* **2012**, *14*, 10690–10704.

(85) Ganyushin, D.; Gilka, N.; Taylor, P. R.; Marian, C. M.; Neese, F. The Resolution of the Identity Approximation for Calculations of Spin–Spin Contribution to Zero–Field Splitting Parameters. *J. Chem. Phys.* **2010**, *132*.

(86) Neese, F. Efficient and Accurate Approximations to the Molecular Spin–Orbit Coupling Operator and their use in Molecular G–Tensor Calculations. *J. Chem. Phys.* **2005**, *122*.

(87) Koseki, S.; Schmidt, M. W.; Gordon, M. S. Effective Nuclear Charges for the First– Through Third–Row Transition Metal Elements in Spin–Orbit Calculations. *J. Phys. Chem. A* **1998**, *102*, 10430–10435.

(88) Zare, R. N.; Harter, W. G. Angular Momentum: Understanding Spatial Aspects in Chemistry and Physics. *New York* **1988**, *120*.

(89) Hirata, S.; Head-Gordon, M. Time–Dependent Density Functional Theory Within the Tamm–Dancoff Approximation. *Chem. Phys. Lett.* **1999**, *314*, 291–299.

(90) Bellonzi, N.; Medders, G. R.; Epifanovsky, E.; Subotnik, J. E. Configuration Interaction Singles With Spin-Orbit Coupling: Constructing Spin-Adiabatic States and Their Analytical Nuclear Gradients. *J. Chem. Phys.* **2019**, *150*.

(91) Bellonzi, N.; Alguire, E.; Fatehi, S.; Shao, Y.; Subotnik, J. E. TD-DFT Spin-Adiabats with Analytic Nonadiabatic Derivative Couplings. *J. Chem. Phys.* **2020**, *152*.

(92) Crespo-Otero, R.; Barbatti, M. Spectrum Simulation and Decomposition with Nuclear Ensemble: Formal Derivation and Application to Benzene, Furan and 2–Phenylfuran. *Marco Antonio Chaer Nascimento: A Festschrift from Theoretical Chemistry Accounts* **2014**, 89–102.

(93) Barbatti, M.; Aquino, A. J.; Lischka, H. The UV Absorption of Nucleobases: Semi-

Classical ab initio Spectra Simulations. *Phys. Chem. Chem. Phys.* **2010**, *12*, 4959–4967.

(94) Sršeň, v.; Sita, J.; Slavíček, P.; Ladányi, V.; Heger, D. Limits of the Nuclear Ensemble Method for Electronic Spectra Simulations: Temperature Dependence of the (E)–Azobenzene Spectrum. *J. Chem. Theory Comput.* **2020**, *16*, 6428–6438.

(95) Marcus, R. A. Electron Transfer Reactions in Chemistry: Theory and Experiment (Nobel lecture). *Angew. Chem., Int. Ed. Engl.* **1993**, *32*, 1111–1121.

(96) Marian, C. M. Spin–Orbit Coupling and Intersystem Crossing in Molecules. *Wiley Interdiscip. Rev. Comput. Mol. Sci.* **2012**, *2*, 187–203.

(97) Ou, Q.; Subotnik, J. E. Electronic Relaxation in Benzaldehyde Evaluated via TD-DFT and Localized Diabatization: Intersystem Crossings, Conical Intersections, and Phosphorescence. *J. Phys. Chem. C* **2013**, *117*, 19839–19849.

(98) Liu, Y.; Lin, M.; Zhao, Y. Intersystem Crossing Rates of Isolated Fullerenes: Theoretical Calculations. *J. Phys. Chem. A* **2017**, *121*, 1145–1152.

(99) Epifanovsky, E. et al. Software for the frontiers of quantum chemistry: An overview of developments in the Q-Chem 5 package. *J. Chem. Phys.* **2021**, *155*, 084801.

(100) Kirketerp, M.-B. S.; Nielsen, S. B. Absorption Spectrum of Isolated tris(2,2'–bipyridine) ruthenium (II) Dications in Vacuo. *Int. J. Mass Spectrom.* **2010**, *297*, 63–66.

(101) Closser, K. D.; Gessner, O.; Head-Gordon, M. Simulations of the Dissociation of Small Helium Clusters with ab initio Molecular Dynamics in Electronically Excited States. *J. Chem. Phys.* **2014**, *140*.

(102) Heully, J.-L.; Alary, F.; Boggio-Pasqua, M. Spin–Orbit Effects on the Photophysical Properties of $Ru(bpy)_3{}^{2+}$. *J. Chem. Phys.* **2009**, *131*.

(103) Demas, J.; Taylor, D. On the "intersystem crossing" yields in ruthenium (II) and osmium (II) photosensitizers. *Inorg. Chem.* **1979**, *18*, 3177–3179.

(104) Talbot, J. J.; Head-Gordon, M.; Cotton, S. J. The Symmetric Quasi-Classical Model Using on-the-fly Time-Dependent Density Functional Theory Within the Tamm–Dancoff Approximation. *Mol. Phys.* **2023**, *121*, e2153761.

(105) Herbert, J. M.; Lange, A. W.; Cui, Q.; Ren, P.; Meuwly, M. *Many-Body Effects and Electrostatics in Biomolecules*; Pan Stanford, 2016; pp 363–416.

TOC Graphic

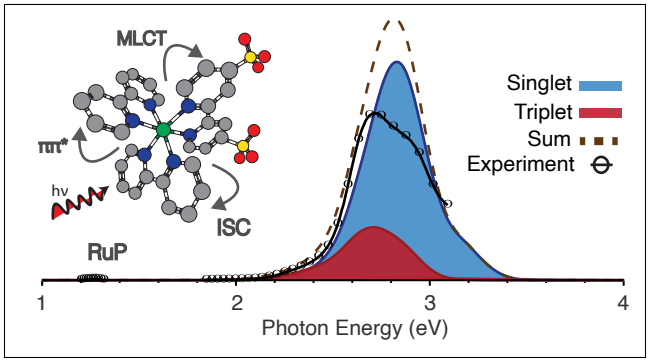
MLCT
ππ*
hv
ISC
RuP
Singlet
Triplet
Sum
Experiment
1
2
3
4
Photon Energy (eV)

Supporting Information:

The Role of Spin-Orbit Coupling in the Linear Absorption Spectrum and Intersystem Crossing Rate Coefficients of Ruthenium Polypyridyl Dyes

Justin J. Talbot,[†] Thomas P. Cheshire,[‡] Stephen J. Cotton,[†] Frances A. Houle,[‡] and Martin Head-Gordon*[,†]

†*Department of Chemistry, University of California, Berkeley, California 94720, United States*

‡*Chemical Sciences Division, Lawrence Berkeley National Laboratory, Berkeley, California, 94720, United States*

E-mail: mhg@cchem.berkeley.edu

Electronic Structure Benchmarks

An investigation into the basis set and functional dependence of the MLCT transitions for RuBPY is presented in Fig. S1. The experimentally measured peak energy ($\Delta E = 2.883$ eV)[1] was used as a benchmark. The lowest energy pair with the greatest oscillator strength (see inset) was analyzed against a set of generalized gradient (GGA), global hybrid (h-GGA), and range-separated hybrid (rsh-GGA) density functionals. The SG-2 grid was used for all calculations.[2] In general, the density functionals from each rung follow a similar trend. The GGA tends to underestimate the MLCT excitation energy while range-separated and hybrid functionals tend to overestimate this quantity. The lowest absolute error was found with B3LYP and this functional was used for all calculations. The selection of the B3LYP functional reflects its superior performance for this problem. This can seen from the excellent agreement between the calculated and measured linear absorption spectrum in the main text. In general this is not the case and previous work comparing TDDFT excitations across different rungs of density functionals show that B3LYP has an RMSE of 0.467 eV for singlet excitations and 0.399 eV for triplet excitations.[3]

Perturbative Calculations

For each of the dye molecules studied here, the triplet manifold is lower in energy than the singlet manifold. The higher-lying states (i.e., S_{10} and T_{10}) are ≈ 0.5 eV higher in energy than the overlapping transitions in the MLCT bands. A table of the spin-pure and SOC transition energies is shown in Table S1. Since these states do not couple through SOC to each other or to other states in the MLCT band, as evidenced by the near degeneracies between the spin-pure and SOC transition energies, all states above them were excluded from the BP calculations.

The effective nuclear charges (in a.u.) used in the BP Hamiltonian are provided in Table S2. The effective charge for ruthenium was calculated following the procedure outlined in Ref. 4. The main group element effective charges were taken from the table in Ref. 5.

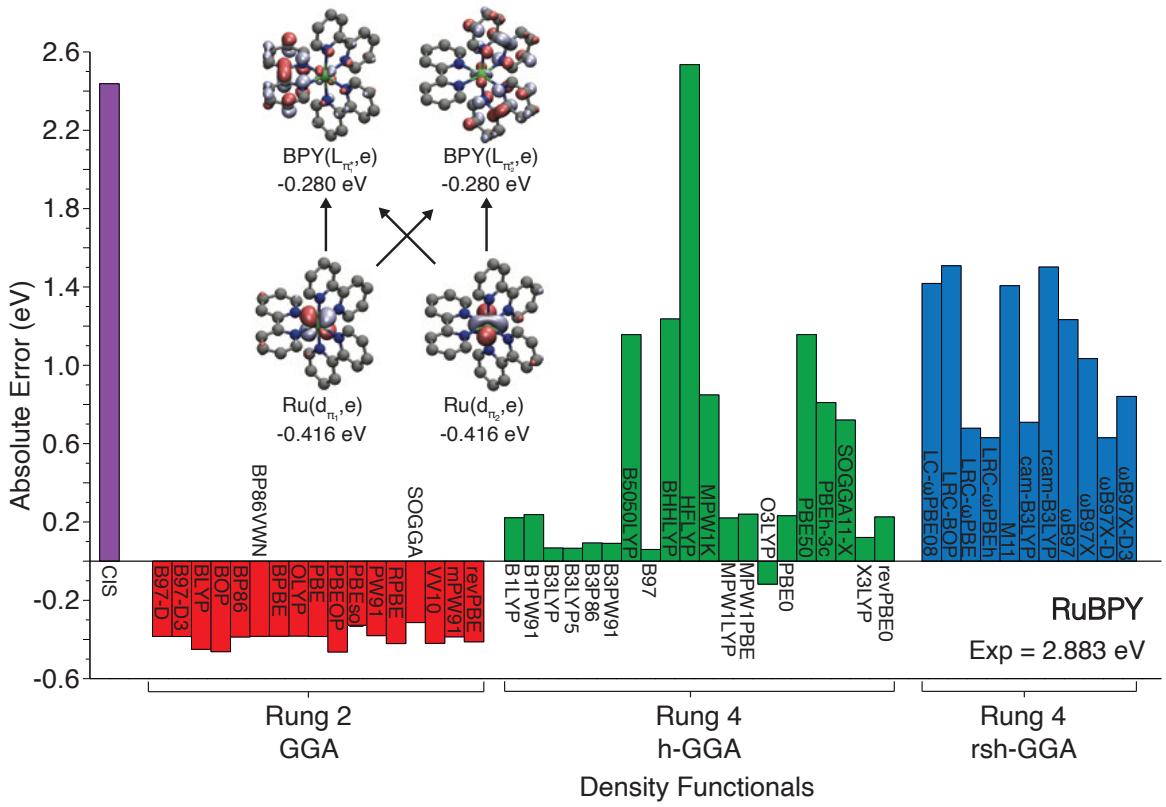

Fig. S1: Comparison between the calculated def2-SVP-PP MLCT excitation energies and experiment for RuBPY. Three different rungs of density functionals were benchmarked including generalized gradient (GGA), global hybrid (h-GGA), and range-separated hybrid (rsh-GGA). The configuration interaction singles (CIS) value is shown in purple. The inset shows the B3LYP occupied π (bottom) and virtual π^* (top) orbitals involved in the transition. The isosurface value is ± 0.05 au.

Table S1: Excitation energies at the equilibrium ground electronic state geometries for S_{10} and T_{10}. The first two columns contain the spin-pure transitions (i.e., the transitions not including SOC). Note that the spin-pure triplet transition energies are three-fold degenerate. The last two columns contain the SOC transitions.

	spin-pure		SOC	
Dye	S_{10} **(eV)**	T_{10} (eV)	S_{10} (eV)	T_{10} $m = 0, \pm 1$ (eV)
RuBPY	3.4169	3.3076	3.4206	3.3150, 3.3127, 3.3118
RuP	3.4145	3.2851	3.4157	3.2870, 3.2868, 3.2865
RuP2	3.4064	3.2665	3.4072	3.2678, 3.2678, 3.2676
RuP3	3.4083	3.2643	3.4092	3.2657, 3.2656, 3.2654

Table S2: The screened nuclear charges (a.u.) used for the perturbative Breit-Pauli spin-orbit calculations.

Atom	Charge
Ru	206.24
C	3.90
N	4.90
P	180.0
O	6.00
H	1.00

Additional Orbital Analysis

Some additional orbital and SOC analysis for RuBPY, RuP, RuP2, and RuP3 is provided in Figs. S2 – S5 respectively. The right panels show the frontier molecular orbitals for each dye. The left panels compare the spin-pure excitation energies (i.e., not including SOC) on the y-axis against the SOC excitation energies. There are nine singlet states with $m = 0$ and 27 triplet states (i.e., nine three-fold degenerate spin-pure triplet states with $m = 0, \pm 1$). The impulse plots are the SOC oscillator strengths (with numerical values on the y2 axis) which have been color-coded and assigned to primary orbital transitions. Each dye follows a similar trend with the bright oscillator strengths corresponding to $d_\pi \rightarrow \pi^*$ transitions and

the much weaker oscillator strenghts assigned to $d_\pi \rightarrow L^*$ transitions.

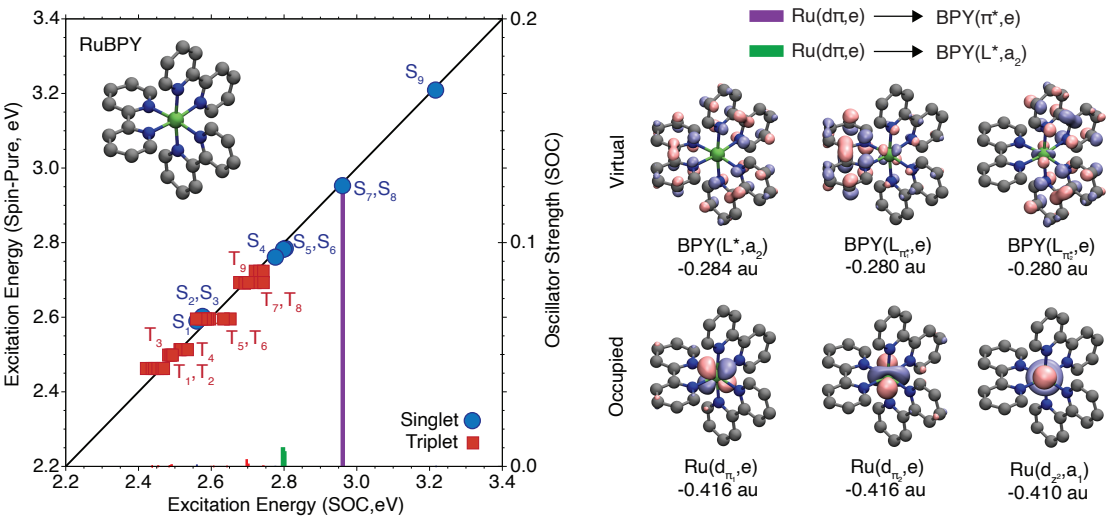

Fig. S2: The MLCT transitions of RuBPY (left). The spin-pure excitation energies (y-axis) and the spin-orbit coupled excitation energies (x-axis) for the lowest nine singlet (blue circles) and 27 triplet states (red squares) evaluated at the minimum energy geometries. The impulse plots correspond to the spin-orbit coupled oscillator strengths which are shown on the y2-axis. All excitation energies are in eV. The frontier molecular orbitals of RuBPY (right). Orbital energies (in au) and symmetries (D_3) are displayed below each orbital. The color bars represent the primary contributing orbital transitions. The isosurface value is ± 0.05 au.

Intersystem Crossing Rate Coefficients

The state-specific weighted intersystem crossing rate coefficients (s^{-1}) calculated using Eq. 16 of the main text are provided in Table S3. The SOC oscillator strengths are listed as f_{osc}. The rate coefficients are weighted by the normalized oscillator strengths including only S_5 – S_8 for each dye molecule. The total rate for each dye molecule is the sum of the normalized oscillator strength weighted columns. A depiction of the variables used in Eq. 16 and Eq. 18 of the main text, under the harmonic, vertical, and parallel gradient approximations, is shown in Fig. S6.

A single imaginary mode was removed from the the rate coefficient calculations on S_8 for RuBPY. The first justification for removing this mode was that it was found to have a small vibrational frequency ($\omega = 185i$ cm^{-1}). As shown in Fig. S7, the potential energy

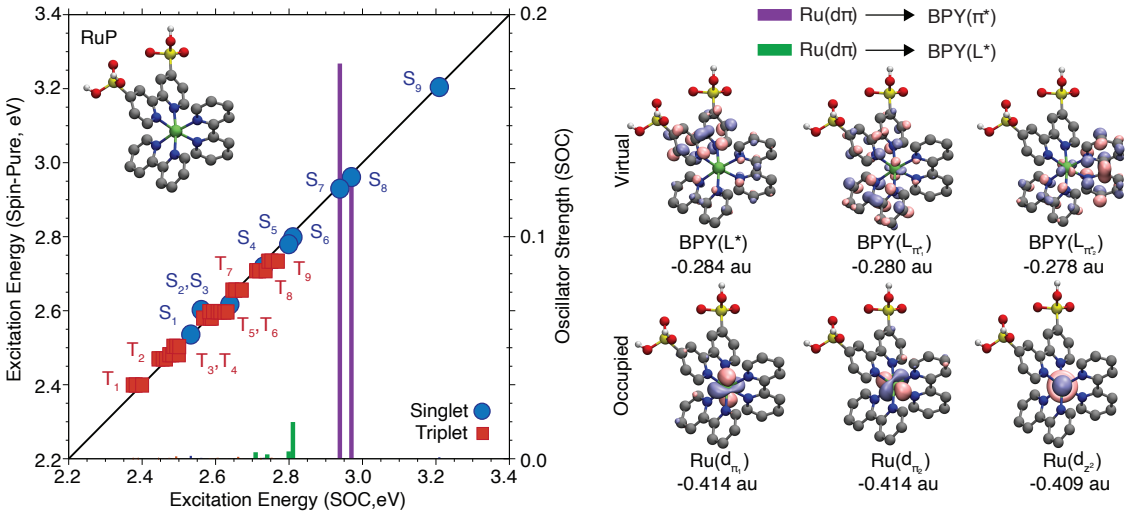

Fig. S3: The MLCT transitions of RuP (left). The spin-pure excitation energies (y-axis) and the spin-orbit coupled excitation energies (x-axis) for the lowest nine singlet (blue circles) and 27 triplet states (red squares) evaluated at the minimum energy geometries. The impulse plots correspond to the spin-orbit coupled oscillator strengths which are shown on the y2-axis. All excitation energies are in eV. The frontier molecular orbitals of RuP (right). Orbital energies (in au) are displayed below each orbital. The color bars represent the primary contributing orbital transitions. The isosurface value is ±0.05 au.

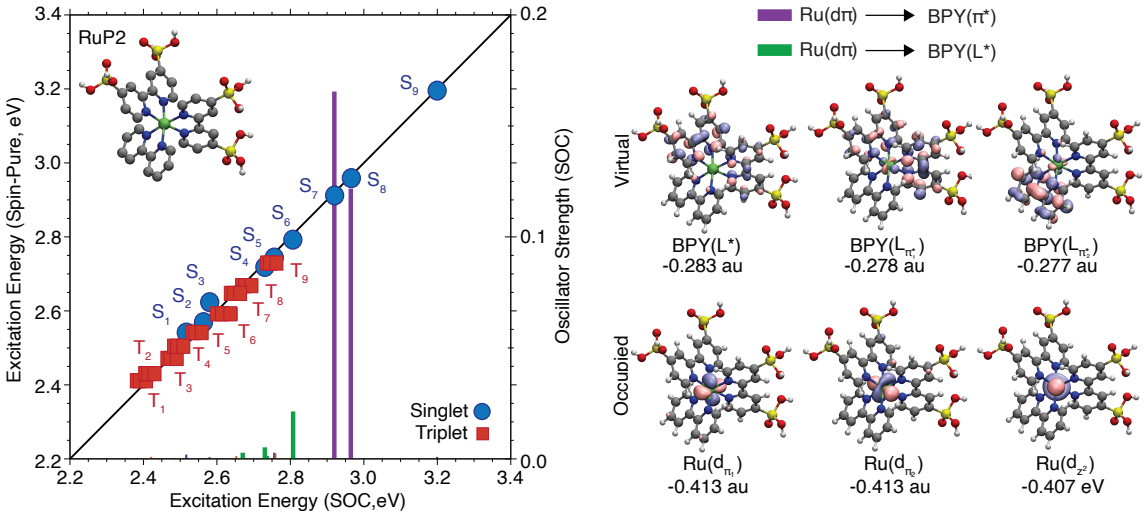

Fig. S4: The MLCT transitions of RuP2 (left). The spin-pure excitation energies (y-axis) and the spin-orbit coupled excitation energies (x-axis) for the lowest nine singlet (blue circles) and 27 triplet states (red squares) evaluated at the minimum energy geometries. The impulse plots correspond to the spin-orbit coupled oscillator strengths which are shown on the y2-axis. All excitation energies are in eV. The frontier molecular orbitals of RuP2 (right). Orbital energies (in au) are displayed below each orbital. The color bars represent the primary contributing orbital transitions. The isosurface value is ±0.05 au.

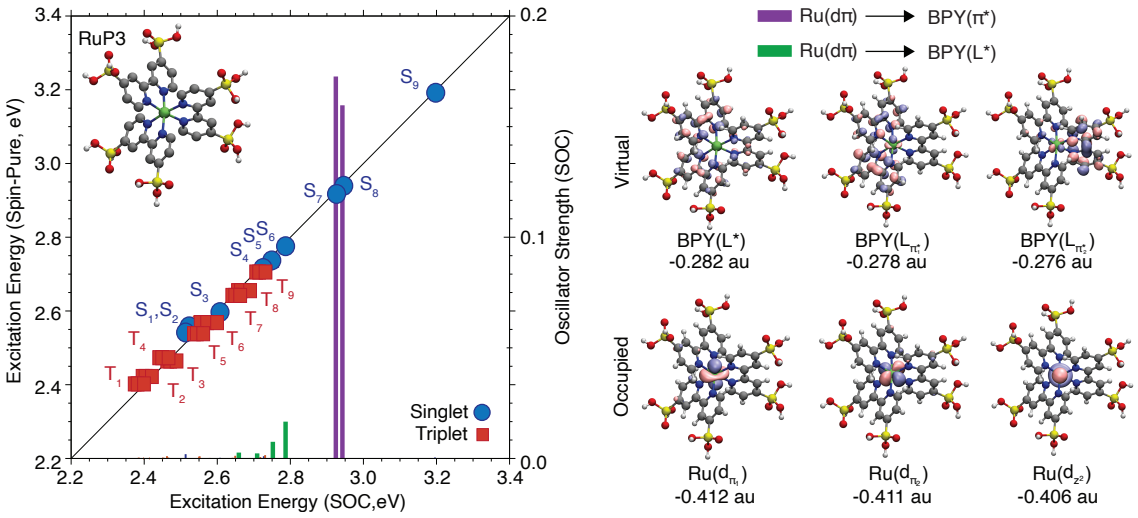

Fig. S5: The MLCT transitions of RuP3 (left). The spin-pure excitation energies (y-axis) and the spin-orbit coupled excitation energies (x-axis) for the lowest nine singlet (blue circles) and 27 triplet states (red squares) evaluated at the minimum energy geometries. The impulse plots correspond to the spin-orbit coupled oscillator strengths which are shown on the y2-axis. All excitation energies are in eV. The frontier molecular orbitals of RuP3 (right). Orbital energies (in au) are displayed below each orbital. The color bars represent the primary contributing orbital transitions. The isosurface value is ±0.05 au.

Table S3: The weighted intersystem crossing rate coefficients in s^{-1} for RuBPY, RuP, RuP2, and RuP3. The oscillator strengths have been normalized such that the sum is unity. The rate coefficients are color coded according to the fastest (red) and slowest (green). The total rate is the sum of the weighted columns. For the S_8 column of RuBPY, one imaginary frequency and mode was removed from the calculations (see below).

	RuBPY				RuP				RuP2				RuP3			
	S5	S6	S7	S8	S5	S6	S7	S8	S5	S6	S7	S8	S5	S6	S7	S8
T1	2.25E+12	2.20E+12	1.91E+12	4.50E+10	1.67E+12	3.62E+12	4.39E+12	2.29E+10	9.46E+11	4.49E+12	1.14E+13	8.65E+12	1.75E+12	3.04E+12	1.43E+12	1.34E+12
T2	7.81E+11	6.10E+11	1.22E+05	1.62E+10	8.05E+11	9.03E+11	9.66E+08	3.51E+01	2.41E+11	1.50E+12	6.94E+06	1.42E+01	6.82E+11	5.29E+11	7.97E+03	9.71E+03
T3	1.77E+10	5.64E+06	6.04E+12	6.96E+00	2.54E+07	1.66E+08	1.18E+13	7.65E+11	8.28E+06	3.74E+09	6.87E+07	7.03E+09	1.59E+08	3.78E+07	3.56E+12	2.96E+12
T4	2.97E+09	4.59E+09	2.13E+11	1.78E+11	5.47E+09	1.07E+10	6.85E+11	4.46E+11	1.83E+09	1.86E+10	4.44E+09	8.88E+10	2.47E+09	7.10E+09	6.19E+10	4.99E+10
T5	6.85E+09	5.58E+09	4.41E+08	1.20E−02	8.02E+09	2.58E+10	8.80E+11	5.57E+05	3.25E+09	3.52E+10	1.80E+09	6.67E+10	6.55E+09	1.95E+10	1.18E+08	7.70E+07
T6	6.03E+09	4.78E+09	2.36E+05	2.92E+06	3.51E+09	8.71E+09	9.88E+10	6.92E−02	9.48E+08	2.00E+10	1.48E+12	7.19E+11	2.69E+09	1.12E+10	7.52E+03	8.99E+03
T7	9.45E+08	7.08E+08	5.21E+08	3.70E+05	1.06E+09	2.83E+09	1.22E+11	8.88E+01	2.70E+08	6.22E+09	1.16E+10	1.16E+10	6.06E+08	1.27E+09	2.07E+05	1.51E+05
T8	6.31E+08	4.74E+08	6.81E+11	7.53E+11	1.33E+09	5.33E+09	2.00E+12	4.61E+12	5.71E+08	5.83E+09	3.80E+11	3.73E+11	5.38E+08	1.75E+09	6.78E+11	5.87E+11
T9	2.71E+07	1.79E+06	9.52E+11	3.20E+11	2.39E+08	9.01E+08	1.79E+12	9.19E+10	4.84E+07	1.34E+09	1.30E+12	1.25E+12	8.68E+07	4.09E+07	8.72E+11	7.51E+11
T10	5.81E+02	5.54E+02	1.24E+09	3.03E+04	5.70E+02	3.94E+03	4.43E+09	3.50E+08	1.25E+02	3.16E+03	7.87E+09	6.36E+09	2.85E+02	1.92E+03	5.01E+09	4.98E+09
fosc.	9.36E−03	9.02E−03	1.28E−01	1.28E−01	7.38E−03	1.66E−02	1.50E−01	1.30E−01	4.94E−03	2.30E−02	1.59E−01	1.47E−01	1.01E−02	1.75E−02	1.73E−01	1.74E−01
Weight	3.41E−02	3.29E−02	4.66E−01	4.67E−01	2.43E−02	5.47E−02	4.94E−01	4.27E−01	1.48E−02	6.87E−02	4.76E−01	4.40E−01	2.70E−02	4.67E−02	4.62E−01	4.64E−01
Sum	3.07E+12	2.83E+12	9.79E+12	1.31E+12	2.49E+12	4.57E+12	2.18E+13	5.93E+12	1.19E+12	6.09E+12	1.46E+13	1.12E+13	2.44E+12	3.61E+12	6.61E+12	5.70E+12
Total	1.70E+13				3.48E+13				3.31E+13				1.84E+13			

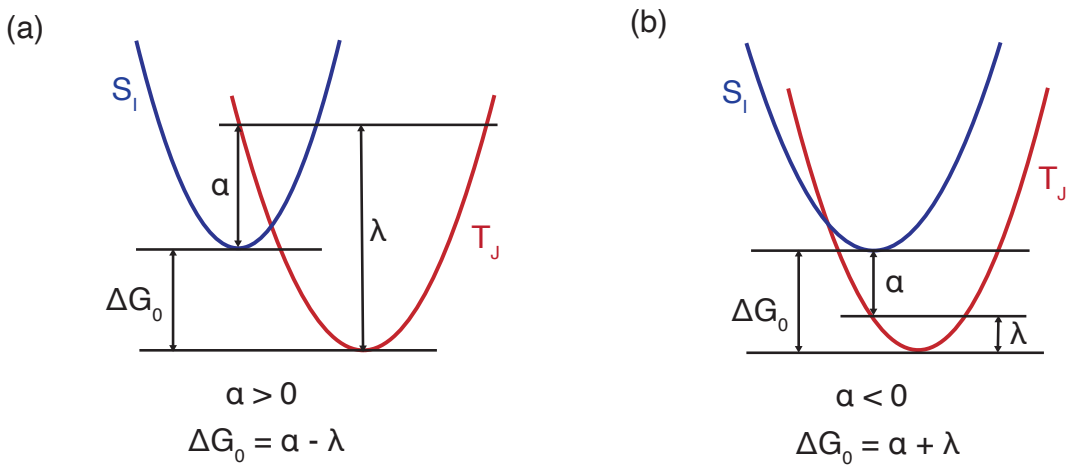

Fig. S6: The definition of the driving force ΔG_0 and the reorganization energy λ for intersystem crossing between an initial singlet state S_I and a final triplet state T_J. α denotes the excitation (or de-excitation) energy. (a) The case when α is positive. (b) The case when α is negative.

surface along this mode is symmetric around the saddle point and the energy *increases* for displacements greater than $Q = \pm 0.02$Å. The energy difference is ΔE = E($Q = \pm 0.02$) - E($Q = 0.0$) = 0.002 kcal/mol which suggests that this mode may result as a numerical artifact of the electronic structure calculations (i.e., the mode possibly arises from a grid/threshold error).

Linear Absorption Cross Section Analysis

The cross sections reported in main text have not been shifted and the harmonic oscillator Wigner parameters (i.e., the harmonic frequencies and reduced masses) were calculated using B3LYP (without scaling factors) from the optimized ground-electronic state geometries. The width of the cross sections are controllable with the parameter δ from Eq. 15 of the main text. This was set to $\delta = 0.1$ eV following Ref. 6, however this is a conservative estimate of the FWHM of the underlying Gaussian transitions. In our previous work on the kinetics of these dyes (from the analysis in Ref. 7), we estimated that the FWHM was ≈ 0.2 eV. For comparison, plots of the cross sections with $\delta = 0.2$ eV are shown in Fig. S8.

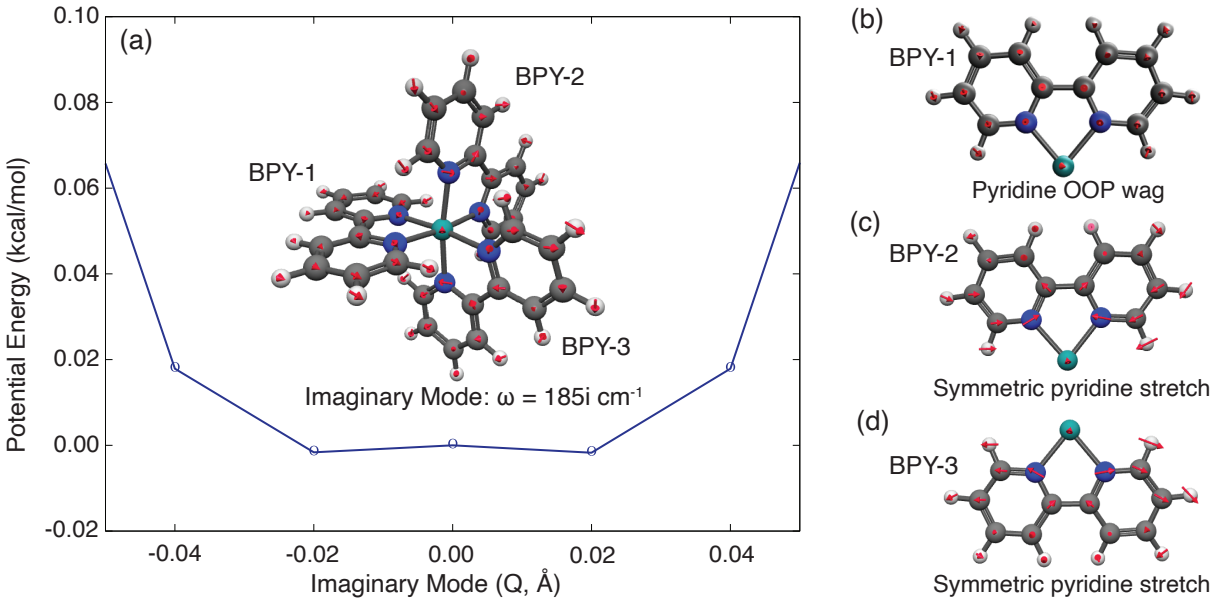

Fig. S7: (a) The potential energy surface along the imaginary mode ($\omega = 185i$ cm^{-1}) on the S_8 electronic state of RuBPY. A depiction of the mode is shown in the inset. The mode can be described as a an out-of-plane (OOP) wagging motion the first bipyridine ligand (labeled BP-1 (b)) and a symmetric stretching of two pyridine ligands (labeled BPY-2 (c) and BPY-3 (d)).

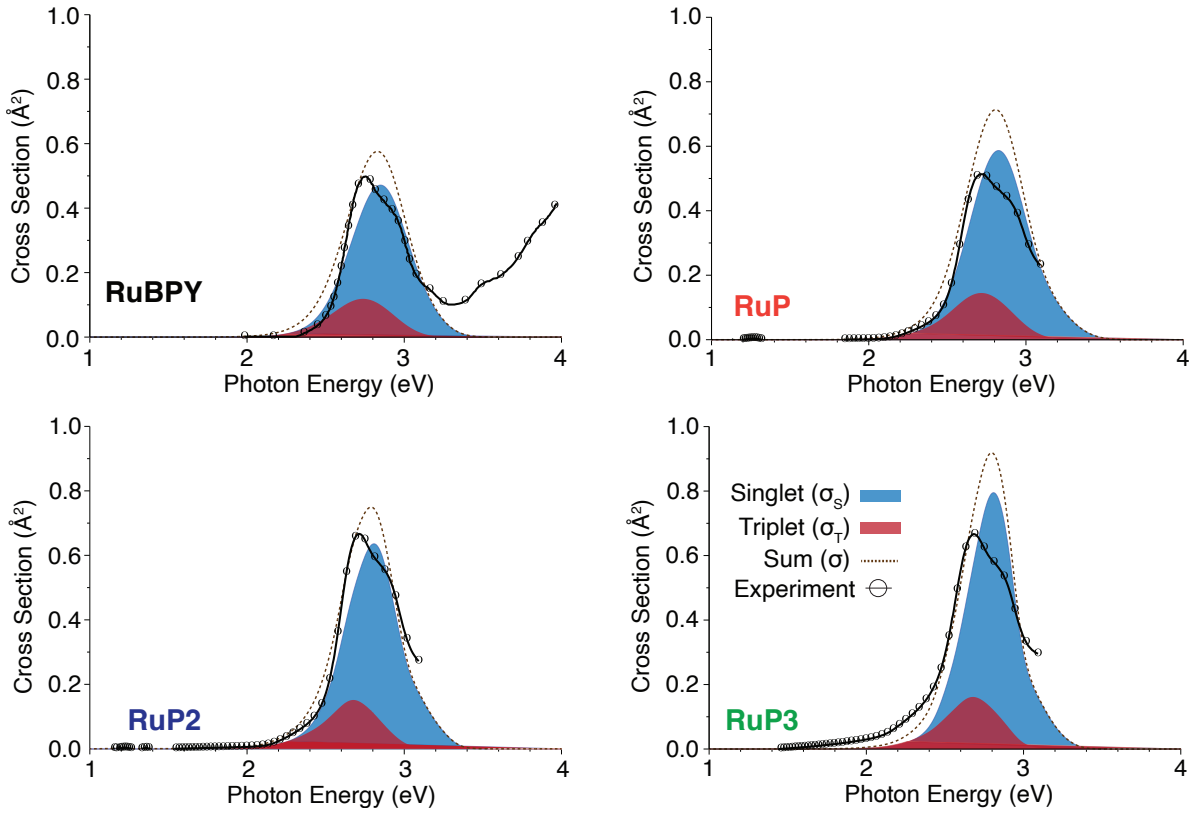

Fig. S8: A comparison between the experimental and simulated linear absorption cross sections (Å^2) with $\delta = 0.2$ eV for RuBPY (top left), RuP (top right), RuP2 (bottom left) and RuP3 (bottom right). All energies are in (eV). The experimental linear absorption cross sections are shown with open circles.

References

(1) Kirketerp, M.-B. S.; Nielsen, S. B. Absorption Spectrum of Isolated tris(2,2'–bipyridine) ruthenium (II) Dications in Vacuo. *Int. J. Mass Spectrom.* **2010**, *297*, 63–66.

(2) Dasgupta, S.; Herbert, J. M. Standard Grids for High-Precision Integration of Modern Density Functionals: SG-2 and SG-3. *J. Comput. Chem.* **2017**, *38*, 869–882.

(3) Liang, J.; Feng, X.; Hait, D.; Head-Gordon, M. Revisiting the Performance of Time-Dependent Density Functional Theory for Electronic Excitations: Assessment of 43 Popular and Recently Developed Functionals From Rungs One to Four. *J. Chem. Theory Comput.* **2022**, *18*, 3460–3473.

(4) Koseki, S.; Schmidt, M. W.; Gordon, M. S. Effective Nuclear Charges for the First– Through Third–Row Transition Metal Elements in Spin–Orbit Calculations. *J. Phys. Chem. A* **1998**, *102*, 10430–10435.

(5) Koseki, S.; Gordon, M. S.; Schmidt, M. W.; Matsunaga, N. Main Group Effective Nuclear Charges for Spin-Orbit Calculations. *J. Phys. Chem.* **1995**, *99*, 12764–12772.

(6) Crespo-Otero, R.; Barbatti, M. Spectrum Simulation and Decomposition with Nuclear Ensemble: Formal Derivation and Application to Benzene, Furan and 2–Phenylfuran. *Marco Antonio Chaer Nascimento: A Festschrift from Theoretical Chemistry Accounts* **2014**, 89–102.

(7) Cheshire, T. P.; Brennaman, M. K.; Giokas, P. G.; Zigler, D. F.; Moran, A. M.; Papanikolas, J. M.; Meyer, G. J.; Meyer, T. J.; Houle, F. A. Ultrafast Relaxations in Ruthenium Polypyridyl Chromophores Determined by Stochastic Kinetics Simulations. *J. Phys. Chem. B* **2020**, *124*, 5971–5985.